潘凌云

电话：18807143071　　邮箱：19222013@bjtu.edu.cn　　籍贯：湖北武汉

教育背景

本科：北京交通大学（机械电子）　　研究生（预录取）：清华大学机械专业硕士（智能装备设计与制造）

- **年级排名：2/57　GPA：3.91/4**
- **核心课程：微积分 I（99）、微积分 II（100）、概率论与数理统计（97）、线性代数（90）、C 语言（97）、大学物理（100）、机器动力学（97）、机械零件设计基础（92）、机械制造（93）**
- **英语水平：CET4：609、CET6：560、IELTS：7.0**
- **专业技能：**编程软件: Dev-C++, VScode, Pycharm, VMware, MATLAB, KEIL 等；建模软件: AutoCAD, Inventor, SolidWorks 等；分析软件: Fluent, ANSYS, SPSS, LINGO, jamovi 等；

科研经历

2022.10　　基于深度学习的铁路货车故障识别系统研究

- **本科毕业设计**
- 设计了定位（目标检测网络实现）+识别（图像分类网络实现）的二阶段整体方案。
- 针对 TFDS 光照不均问题设计了 Retinex+双边滤波的图像预处理方法；采用改进的 YOLOv5 网络实现零部件分割，达到了定位速度和精度要求；采用改进的 MobileNetv3 网络进行故障分类，达到了故障识别精度要求。

2021.4　　Experimental study on saturation pool boiling heat transfer characteristics of R245fa on the surface covered by sintered copper powder　　二作（导一）

- **依托微细尺度流动与相变北京市重点实验室**
- 论文已发表至 **SCI 一区(JCR)期刊 *Case Studies in Thermal Engineering*（IF=6.268）。**
- 聚焦于高效沸腾传热效果的强化机制研究，揭示多孔层的粒径、层厚等因素的影响机制，为浸没式液冷技术的进一步发展与提升提供基础信息。
- 负责制作实验段以及完成全部的实验流程；使用 EXCEL 进行数据处理；使用 Origin 进行数据可视化；使用 PCC3.3 进行可视化图片处理

2021.4　　Saturated pool boiling heat transfer enhancement of R245fa based on the surface covered by sintered copper powder with and without nanostructure　　三作（导一）

- **依托微细尺度流动与相变北京市重点实验室**
- 论文已发表至 **SCI 一区期刊(JCR) *International Journal of Thermal Sciences***。
- 为进一步提升沸腾传热效果，利用热氧化法在烧结铜粉颗粒表面形成具有超亲水性特性的纳米结构，探究微纳复合结构烧结铜粉多孔层的沸腾传热强化效果。
- 负责完成了全部实验流程；临界热流密度计算、传热系数计算等数据处理工作。

2022.4　　Optimizing the effect of forest carbon sequestration using two models　　负责人

- **获美国大学生数学建模竞赛二等奖**
- 为提升森林的固碳效果，建立动态碳封存模型（DCS），确定最佳的森林轮换周期，并利用数据包络分析法结合 Malmquist 指数评估社会和经济层面的 6 个主要因素的影响，最后采用灰色模型预测 100 年后的固碳量，从而提供一个高效的碳封存方案。
- 负责模型建立、程序编写、论文撰写等工作

竞赛获奖

国家级：全国大学生节能减排社会实践与科技竞赛三等奖
美国大学生数学建模竞赛H奖
省　级：北京市机械创新设计大赛二等奖
校　级：北京交通大学数学竞赛三等奖
北京交通大学机器人方案设计大赛三等奖
北京交通大学机械创新设计大赛三等奖
北京交通大学大学生节能减排社会实践与科技竞赛二等奖

全国推荐免试攻读研究生信息公开暨管理服务系统

> 确认推免资格
> 报名注意事项
> 填报个人信息
1.基本信息
2.个人照片
3.户档信息
4.学习工作信息
5.学籍学历信息
6.学位信息
7.联系信息
8.入伍信息
> 网上交费
> 我的志愿
> 我的复试通知
> 我的待录取通知
> 我的消息

志愿信息

层次：硕士
单位：清华大学
院系：机械工程系
专业：(专业学位)机械（085500）
学习方式：全日制
研究方向：机械专业硕士(智能装备设计与制造)
导师：不区分导师
专项计划类型：非专项计划
就业类型：非定向就业

待录取通知 接受或拒绝待录取通知后，将无法更改。

清华大学 招生办 2022-09-28 17:15

请及时接受待录取通知。

您于9月28日 23:24接受了清华大学的待录取通知

注意事项：

1.请在招生单位规定的时间内通过系统答复是否接受录取通知，否则招生单位可取消待录取通知，未通过系统接受待录取通知的推免生不能被招生单位录取；

2.招生单位发放的待录取通知专业及招生类型（硕士/直博生）可能与报名志愿、复试通知不同，请认真核对后决定是否接受待

北京交通大学 Beijing Jiaotong University

本科生历年学习成绩表

主管部门（盖章）

姓名：潘凌云　学号：19222013　性别：女　出生日期：20001013　民族：汉族

学院：机械与电子控制工程学院　专业：机械电子工程　班级：机械电子1901　学制：四年制　入学日期：20190901

学年学期	课程名称	课类	学分	成绩
2019-2020 第一学期	交通运输概论	限选	1	P
	工程基础	必修	3	B+
	工程材料	必修	4	94
	思想道德修养与法律基础	必修	2.5	B+
	几何与代数(B)	必修	3.5	90
	微积分(B)Ⅰ	必修	6	99
	体育Ⅰ	必修	1	B
	大学生心理学	任选	1	P
2019-2020 第二学期	军事理论	必修	0.5	P
	程序设计	必修	3	97
	电气系统	必修	4	94
	可持续性工程设计	必修	4	92
	中国近现代史纲要	必修	2	A
	思想政治理论课社会实践	必修	1	P
	微积分(B)Ⅱ	必修	5	100
	物理实验Ⅰ	必修	1	A
	排球裁判理论与实践	任选	1	P
2020-2021 第一学期	工程经济与项目管理	任选	2	P
	数字硬件	必修	3	91
	工程训练(A)	必修	3	A
	马克思主义基本原理	必修	2.5	B+
	英语综合能力	限选	12	A
	概率论与数理统计(B)	必修	3.5	97
	工程力学	必修	4	94
	工程物理（A）	必修	5	100
	物理实验Ⅱ	必修	1	A

学年学期	课程名称	课类	学分	成绩
2020-2021 第一学期	巴西柔术	任选	1	P
	学业及职业生涯规划与设计	任选	1	P
2020-2021 第二学期	创新方法	任选	2	P
	固体力学	必修	3	89
	信号与系统	必修	3	96
	机器动力学	必修	4	97
	工程流体力学(英文)	必修	3	92
	热力学工程实验	必修	3	A
	机械电子工程专业认识实习	限选	1	A
	机械产品方案设计综合专题研究	限选	2	A
	毛泽东思想和中国特色社会主义理论体系概论	必修	2	A-
	习近平新时代中国特色社会主义思想概论	必修	2	A
	法语口语入门	任选	2	P
	军事训练	必修	2.5	P
	科技文献检索	任选	1	P
2021-2022 第一学期	电路与系统	必修	3	A
	数字信号处理	必修	3	93
	机器人学和柔性自动化	必修	3	91
	工程设计和管理	必修	3	B+
	机械零件设计基础	必修	4	92
	瑜伽	任选	1	P
	领导力与沟通力	任选	1	P
2021-2022 第二学期	控制原理	必修	3	88
	微控制器结构及应用	必修	3	94
	人机工程学	必修	3	89
	电子学	必修	4	95

学年学期	课程名称	课类	学分	成绩
2022-2023 第一学期	电能利用基础	限选	3	93
	制造工程原理	限选	3	93
	机械电子工程专业生产实习	限选	3	A

学年学期	课程名称	课类	学分	成绩

必修学分	114	限选学分	25	任选学分	13	总学分	152	平均学分绩点	3.91
备注	英语综合能力由-综合评定。								

成绩说明：

百分制	100-90	89-85	84-81	80-78	77-75	74-72	71-68	67-65	64-63	62-60	小于60
五级制	A	A-	B+	B	B-	C+	C	C-	D+	D	F
绩点	4.0	3.7	3.3	3.0	2.7	2.3	2.0	1.7	1.3	1.0	0

（1）课类：必修课、限选课、任选课。
（2）两级制：P，F。“P”仅应用于两级制，且为两级制的最高成绩，采用两级制计载成绩的课程不参与平均学分绩点计算。
（3）平均学分绩点＝Σ（课程绩点*课程学分）/Σ课程学分。

英语成绩

- **四级成绩：606 分**

- **六级成绩：560 分**

- **雅思成绩：7.0 分**

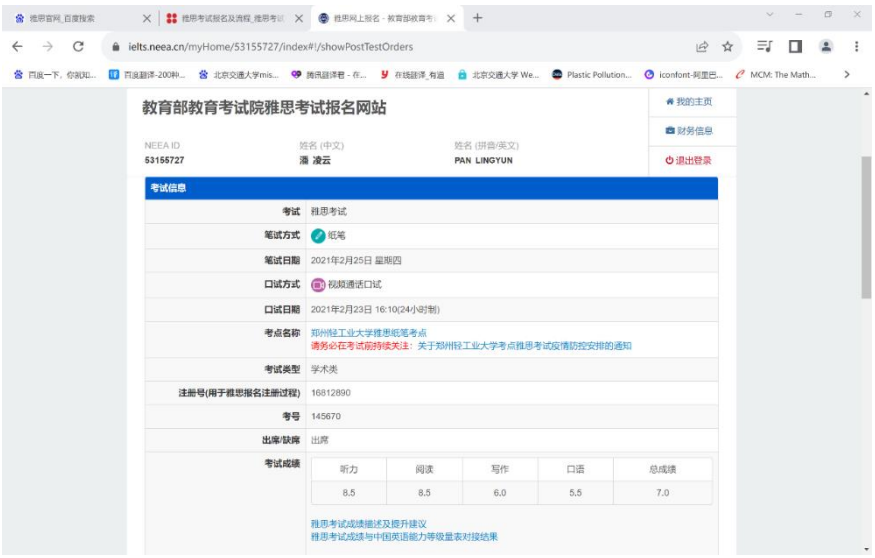

竞赛获奖

➢ 国家级/省部级


“六百光年杯”第十五届
全国大学生节能减排社会实践与科技竞赛
“600 LIGHT YEAR” the 15th National University Student Social Practice and Science Contest on Energy Saving & Emission Reduction
获奖证书
在2022年“六百光年杯”第十五届全国大学生节能减排社会实践与科技竞赛中，经评审，获三等奖。
特发此证，以资鼓励。
参赛院校： 北京交通大学
作品名称： “浸没液冷，更上层楼”基于铜粉颗粒烧结多孔层的高效沸腾传热强化机制研究
作品类型： 科技作品
参赛学生： 潘凌云、闵瑞祺
指导教师： 党超、银了飞
证书编号：2022-03-0796
全国大学生节能减排社会实践与科技竞赛委员会
二〇二二年八月


2022
Interdisciplinary Contest In Modeling®
Certificate of Achievement
Be It Known That The Team Of
Lingyun Pan
With Faculty Advisor
Bingtuan Wang
Or
Beijing Jiaotong University
Was Designated As
Honorable Mention
Solomon Garfunkel, Executive Director
Administered by COMAP With support from
Amanda Beecher, Contest Director
AMS ASA informs MAA siam

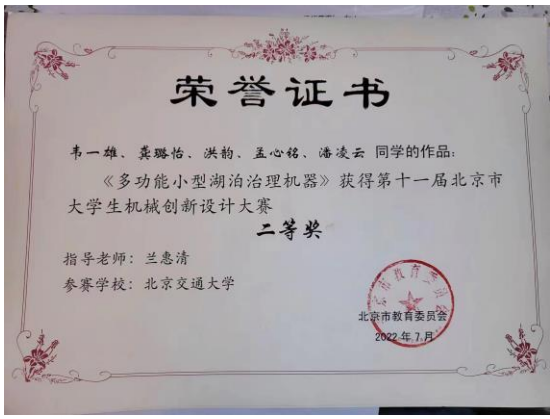
荣誉证书
韦一雄、龚骋怡、洪韵、孟心铭、潘凌云 同学的作品：
《多功能小型湖泊治理机器》获得第十一届北京市大学生机械创新设计大赛
二等奖
指导老师：兰惠清
参赛学校：北京交通大学
北京市教育委员会
2022 年 7 月

➢ 校级


荣誉证书
学　　生：孟心铭、何锦澄、潘凌云、马农杰
作　　品：FH 队
指导教师：感谢
在 2020 年北京交通大学机器人方案设计大赛中荣获三等奖。
特发此证，以资鼓励。
北京交通大学教务处
2020 年 12 月


荣誉证书
潘凌云：
在 2020 年北京交通大学大学生数学竞赛中荣获三等奖。
特发此证，以资鼓励。
北京交通大学教务处
二〇二〇年七月


北京交通大学部处函件
关于公布2021年北京交通大学第十届大学生机械创新设计大赛评审结果的通知


实物组（三等奖，8项）

奖学金


CERTIFICATE OF SCHOLARSHIP
奖学金证书
潘凌云
【学号：19222013】
荣获北京交通大学2019-2020学年
“二等学习优秀奖学金”
特发此证，以资鼓励


CERTIFICATE OF HONOR
荣誉证书
潘凌云
【学号：19222013】
荣获北京交通大学2019-2020学年
“三好学生”荣誉称号
特发此证，以资鼓励


CERTIFICATE OF SCHOLARSHIP
奖学金证书
潘凌云
【学号：19222013】
荣获北京交通大学2019-2020学年
“仁德二等奖学金”
特发此证，以资鼓励

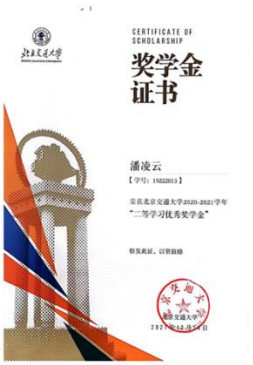
CERTIFICATE OF SCHOLARSHIP
奖学金证书
潘凌云
【学号：19222013】
荣获北京交通大学2020-2021学年
“二等学习优秀奖学金”
特发此证，以资鼓励


CERTIFICATE OF HONOR
荣誉证书
潘凌云
【学号：19222013】
荣获北京交通大学2020-2021学年
“三好学生”荣誉称号
特发此证，以资鼓励

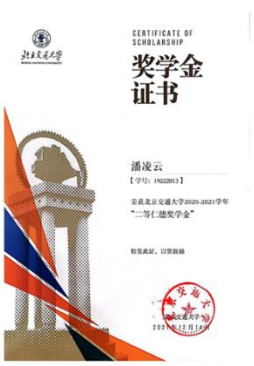
CERTIFICATE OF SCHOLARSHIP
奖学金证书
潘凌云
【学号：19222013】
荣获北京交通大学2020-2021学年
“二等仁德奖学金”
特发此证，以资鼓励

(19)国家知识产权局

(12)实用新型专利

(10)授权公告号 CN 217509561 U
(45)授权公告日 2022.09.30

(21)申请号 202122984151.3

(22)申请日 2021.11.30

(73)专利权人 北京交通大学
地址 100000 北京市海淀区西直门外上园村3号

(72)发明人 潘凌云

(74)专利代理机构 武汉大楚知识产权代理事务所(普通合伙) 42257
专利代理师 徐杨松

(51)Int.Cl.
A01G 23/04(2006.01)
B25J 11/00(2006.01)
B25J 5/02(2006.01)

权利要求书1页 说明书3页 附图2页

(54)实用新型名称

一种可自动种树的爬行机器人

(57)摘要

本实用新型涉及可自动种树的爬行机器人，包括底盘、履带轮、电控旋转台、工作台、运输块、机械手、摆放箱、存放箱、推土模组和浇水模组，底盘两侧均设有履带轮，底盘上连接有电控旋转台，电控旋转台顶端与工作台连接，工作台水平面内部开设有环形槽，环形槽内滑动连接有多个运输块，运输块底端与工作台内部的传动链条固定，工作台一端设有机械手，工作台靠近机械手一侧设有浇水模组，浇水模组两侧均设有推土模组，工作台背离机械手一端设有摆放箱，摆放箱与工作台相连的一侧以及与工作台相邻的其中一侧均开孔，摆放箱与工作台相邻的开孔的外侧在开孔处固定有存放箱。只需人工定期补苗，提高种树效率的同时也节省劳动力。

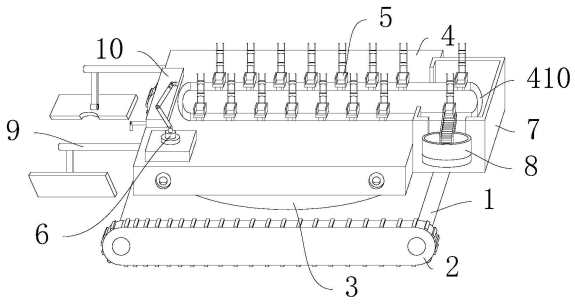

CN 217509561 U

1.一种可自动种树的爬行机器人,其特征在于,包括底盘(1)、履带轮(2)、电控旋转台(3)、工作台(4)、运输块(5)、机械手(6)、摆放箱(7)、存放箱(8)、推土模组(9)和浇水模组(10),所述底盘(1)水平布置,所述底盘(1)两侧均设有履带轮(2),所述底盘(1)上连接有电控旋转台(3),所述电控旋转台(3)顶端与工作台(4)连接,所述工作台(4)水平面内部开设有环形槽(410),所述环形槽(410)内滑动连接有多个运输块(5),所述运输块(5)底端与工作台(4)内部的传动链条固定,所述工作台(4)一端设有机械手(6),所述工作台(4)靠近机械手(6)一侧设有浇水模组(10),所述浇水模组(10)两侧均设有推土模组(9),所述工作台(4)周围固定有多个摄像头,所述工作台(4)背离机械手(6)一端设有摆放箱(7),摆放箱(7)与工作台(4)相连的一侧以及与工作台(4)相邻的其中一侧均开孔,所述摆放箱(7)与工作台(4)相邻的开孔侧的外侧在开孔处固定有存放箱(8),所述存放箱(8)内侧开设有导轨槽(850),所述导轨槽(850)外部固定有运输导轨(840)。

2.根据权利要求1所述的一种可自动种树的爬行机器人,其特征在于,所述运输块(5)顶端开设有放置槽(520),且放置槽(520)的槽壁一侧镂空,所述运输块(5)顶端固定有两根支撑柱(530),所述两根支撑柱(530)之间设有挡片(510)。

3.根据权利要求1所述的一种可自动种树的爬行机器人,其特征在于,所述存放箱(8)内壁底端设有转盘(810),所述转盘(810)外部圆周排列有多块塑料叶片(820),所述存放箱(8)内壁底端靠近运输导轨(840)处设有斜坡(830)。

4.根据权利要求3所述的一种可自动种树的爬行机器人,其特征在于,所述运输导轨(840)内壁底端设有多根滚柱(8410)。

5.根据权利要求1所述的一种可自动种树的爬行机器人,其特征在于,所述工作台(4)一端水平固定有滑杆(11),所述滑杆(11)上套设有两个推土模组(9)。

6.根据权利要求5所述的一种可自动种树的爬行机器人,其特征在于,所述推土模组(9)包括电机(910)、电控升降杆(920)、底座(930)、支架(940)、旋转轴(950)和推土板(960),所述电机(910)套设在滑杆(11)上,所述电机(910)底端固定有电控升降杆(920),所述电控升降杆(920)底端固定有底座(930),所述底座(930)底端固定有支架(940),所述支架(940)与推土板(960)通过旋转轴(950)转动连接。

7.根据权利要求6所述的一种可自动种树的爬行机器人,其特征在于,所述推土板(960)底面与支架(940)平行的方向上设有多个橡胶刷条(970)。

一种可自动种树的爬行机器人

技术领域

[0001] 本实用新型涉及种树机器人领域，具体涉及一种可自动种树的爬行机器人。

背景技术

[0002] 机器人是一种能够半自主或全自主工作的智能机器，机器人具有感知、决策、执行等基本特征，可以辅助甚至代替人类完成为危险、繁重、复杂的工作，提高工作的质量和效率，服务人类生活，扩大或延伸人的活动及能力范围。

[0003] 植树是个繁重的体力活，人工植树填土效率慢，且需要多人配合。

实用新型内容

[0004] 本实用新型所要解决的技术问题是提供一种可自动种树的爬行机器人，以克服上述现有技术中的不足。

[0005] 本实用新型解决上述技术问题的技术方案如下：一种可自动种树的爬行机器人，包括底盘、履带轮、电控旋转台、工作台、运输块、机械手、摆放箱、存放箱、推土模组和浇水模组，底盘水平布置，底盘两侧均设有履带轮，底盘上连接有电控旋转台，电控旋转台顶端与工作台连接，工作台水平面内部开设有环形槽，环形槽内滑动连接有多个运输块，运输块底端与工作台内部的传动链条固定，工作台一端设有机械手，工作台靠近机械手一侧设有浇水模组，浇水模块两侧均设有推土模组，工作台周围固定有多个摄像头，工作台背离机械手一端设有摆放箱，摆放箱与工作台相连的一侧以及与工作台相邻的其中一侧均开孔，摆放箱与工作台相邻的开孔侧的外侧在开孔处固定有存放箱，存放箱内侧开设有导轨槽，导轨槽外部固定有运输导轨。

[0006] 本实用新型的有益效果是：将树苗放在存放箱中，树苗经过运输导轨滑落在摆放箱的运输块上，控制运输块底端的传动链条转速，使树苗落下时，空的运输块正好位于运输导轨下料口，依次接满环形滑槽内所有运输块，转轴和履带轮工作，工作台一侧摄像头自动捕捉周围挖好的树苗坑，控制履带轮行走至指定位置，工作台内部的传动链条带动运输块开始在环形槽内转动，当运输块转动至机械手附近时，控制机械手抓取运输块上的树苗，放入树苗坑中，工作台一侧的推土模组会将外部的土壤推进树苗坑中，然后压实，浇水模组对土壤进行灌溉，机械手收回，履带轮行走至下一工作位置，重复该过程，直至运输块上树苗均被栽种，人工再次补苗，操作简单，可以一人控制多个种树机器人同时工作，提高种树效率的同时也节省劳动力。

[0007] 在上述技术方案的基础上，本实用新型还可以做如下改进。

[0008] 进一步，运输块顶端开设有放置槽，且放置槽的槽壁一侧镂空，运输块顶端固定有两根支撑柱，两根支撑柱之间设有挡片。

[0009] 采用上述进一步的有益效果为：放置槽一侧镂空设计有利于机械手夹持树苗，同时镂空一侧的槽壁略高于放置槽槽底，防止树苗在倾斜放置时从运输块上滑落；运输块顶端的两根支撑柱和挡片可以起到部分支撑作用。

[0010] 进一步，存放箱内壁底端设有转盘，转盘外部圆周排列有多块塑料叶片，存放箱内壁底端靠近运输导轨处设有斜坡。

[0011] 进一步，运输导轨内壁底端设有多根滚柱。

[0012] 采用上述进一步的有益效果为：转盘内部设有旋转电机，可带动转盘以及周围的塑料叶片旋转，当装有树苗的塑料叶片旋转至斜坡时，树苗会由于重力沿着斜坡滑入运输导轨中，操作自动化程度高，不需要人为干预，只需要定期给存放箱补充树苗。

[0013] 进一步，运输导轨内壁底端设有多根滚柱一端水平固定有滑杆，滑杆上套设有两个推土模组。

[0014] 进一步，推土模组包括电机、电控升降杆、底座、支架、旋转轴和推土板，电机套设在滑杆上，电机底端固定有电控升降杆，电控升降杆底端固定有底座，底座底端固定有支架，支架与推土板通过旋转轴转动连接。

[0015] 进一步，推土板底面与支架平行的方向上设有多个橡胶刷条

[0016] 采用上述进一步的有益效果为：控制电机在滑杆上水平移动，同时电控升降杆带动支架底端的推土板下降到土层表面，将土壤刮到树苗坑中，多个橡胶刷条可以增大刮土效率，节省时间；土壤被刮进树苗坑后，推土板将树苗周围土壤包裹，推土板中间开设的树苗孔会将树苗位置空出来，在电控升降杆的作用下，压紧树苗外侧的土层。

附图说明

[0017] 图1为本实用新型所述可自动种树的爬行机器人的结构示意图；

[0018] 图2为图1的部分结构图；

[0019] 图3为图2的局部结构图；

[0020] 图4为图3的俯视图；

[0021] 图5为图1的侧视图。

[0022] 附图中，各标号所代表的部件列表如下：

[0023] 1、底盘，2、履带轮，3、电控旋转台，4、工作台，410、环形槽，5、运输块，510、挡片，520、放置槽，530、支撑柱，6、机械手，7、摆放箱， 8、存放箱，810、转盘，820、塑料叶片，830、斜坡，840、运输导轨，8410、滚柱，850、导轨槽，9、推土模组，910、电机，920、电控升降杆，930、底座，940、支架，950、旋转轴，960、推土板，970、橡胶刷条，10、浇水模组，11、滑杆。

具体实施方式

[0024] 以下结合附图对本实用新型的原理和特征进行描述，所举实例只用于解释本实用新型，并非用于限定本实用新型的范围。

[0025] 实施例1

[0026] 如图1～图5所示，一种可自动种树的爬行机器人，包括；

[0027] 底盘1、履带轮2、电控旋转台3、工作台4、运输块5、机械手6、摆放箱7、存放箱8、推土模组9和浇水模组10，底盘1水平布置，底盘1两侧均设有履带轮2，底盘1上连接有电控旋转台3，电控旋转台3顶端与工作台4连接，工作台4水平面内部开设有环形槽410，环形槽410内滑动连接有多个运输块5，运输块5底端与工作台4内部的传动链条固定，工作台4 一端设有机械手6，工作台4靠近机械手6一侧设有浇水模组10，浇水模块 10两侧均设有推土模组

9，工作台4周围固定有多个摄像头，工作台4背离机械手6一端设有摆放箱7，摆放箱7与工作台4相连的一侧以及与工作台 4相邻的其中一侧均开孔，摆放箱7与工作台4相邻的开孔侧的外侧在开孔处固定有存放箱8，存放箱8内侧开设有导轨槽850，导轨槽850外部固定有运输导轨840。

[0028] 电控旋转台3可根据不同需求旋转不同角度。

[0029] 实施例2

[0030] 如图1～图5所示，本实施例为在实施例1的基础上所进行的进一步改进，其具体如下：

[0031] 运输块5顶端开设有放置槽520，且放置槽520的槽壁一侧镂空，运输块5顶端固定有两根支撑柱530，两根支撑柱530之间设有挡片510。

[0032] 放置槽520槽底均铺设有柔性垫片，减少树苗底部刮伤，提高树苗的成活率。

[0033] 实施例3

[0034] 如图1～图5所示，本实施例为在实施例1的基础上所进行的进一步改进，其具体如下：

[0035] 存放箱8内壁底端设有转盘810，转盘810外部圆周排列有多块塑料叶片820，存放箱8内壁底端靠近运输导轨840处设有斜坡830。

[0036] 运输导轨840内壁底端设有多根滚柱8410。

[0037] 滚柱8410表面和运输导轨840内槽均采用光滑材料制作，减小与树苗根部的摩擦，保护树苗。

[0038] 实施例4

[0039] 如图1～图5所示，本实施例为在实施例1的基础上所进行的进一步改进，其具体如下：

[0040] 工作台4一端水平固定有滑杆11，滑杆11上套设有两个推土模组9。

[0041] 推土模组9包括电机910、电控升降杆920、底座930、支架940、旋转轴950和推土板960，电机910套设在滑杆11上，电机910底端固定有电控升降杆920，电控升降杆920底端固定有底座930，底座930底端固定有支架940，支架940与推土板960通过旋转轴950转动连接。

[0042] 推土板960底面与支架940平行的方向上设有多个橡胶刷条970。

[0043] 橡胶刷条970为可更换式橡胶条，定期更换橡胶条，防止橡胶条老化磨损严重，刮土效率低。

[0044] 尽管上面已经示出和描述了本实用新型的实施例，可以理解的是，上述实施例是示例性的，不能理解为对本实用新型的限制，本领域的普通技术人员在本实用新型的范围内可以对上述实施例进行变化、修改、替换和变型。

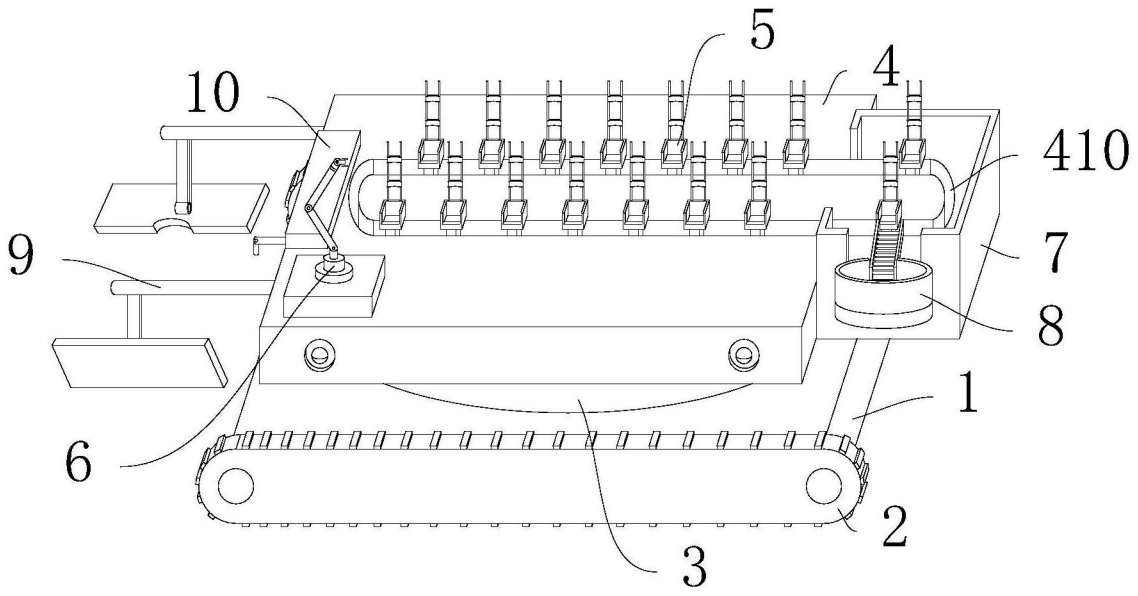

图1

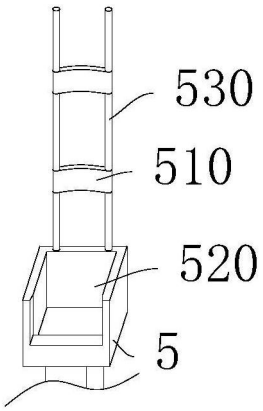

图2

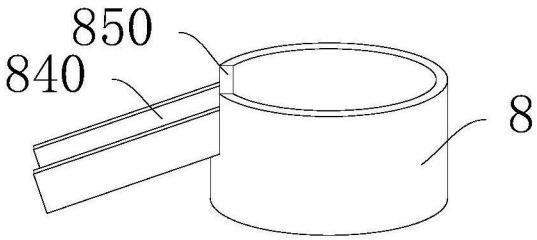

图3

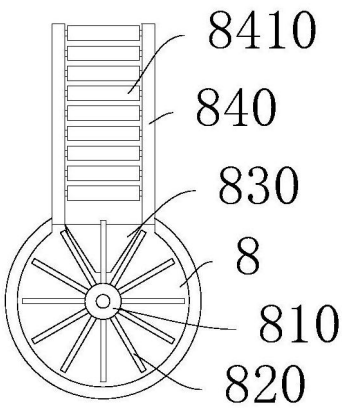

图4

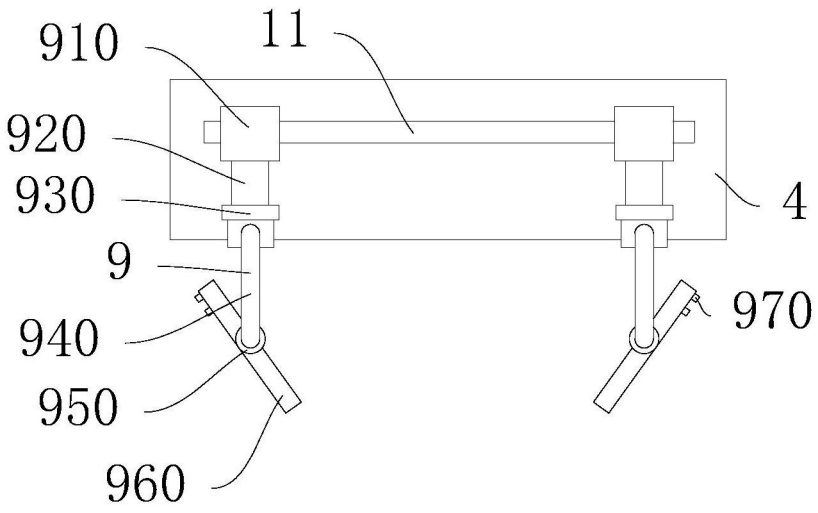

图5

Case Studies in Thermal Engineering 37 (2022) 102223

Contents lists available at ScienceDirect

Case Studies in Thermal Engineering

journal homepage: www.elsevier.com/locate/csite

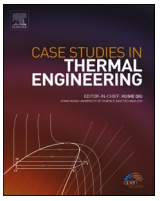

Experimental study on saturation pool boiling heat transfer characteristics of R245fa on the surface covered by sintered copper powder

Chao Dang [a], Lingyun Pan [a], Ruiqi Min [a], Liaofei Yin [a,b,*], Yi Ding [a], Hongwei Jia [c]

[a] Beijing Key Laboratory of Flow and Heat Transfer of Phase Changing in Micro and Small Scale, Beijing Jiaotong University, Beijing, 100044, China
[b] Key Laboratory of Thermal Science and Power Engineering of Ministry of Education, Department of Energy and Power Engineering, Tsinghua University, Beijing, 100084, China
[c] School of Environmental Science and Engineering, Donghua University, Shanghai, 201620, China

ARTICLE INFO

Keywords:
Pool boiling
Refrigerant R245fa
Sintered copper powder
Heat transfer enhancement
Visualization

ABSTRACT

In this paper, the mechanism of pool boiling heat transfer enhancement on the surface covered with sintered copper powder porous layer has been investigated. The refrigerant R245fa with great application prospect in electronic cooling field was selected as the test fluid. According to the results, the boiling heat transfer performance of R245fa could be effectively enhanced by attaching the sintered copper powder porous layer to the plain copper surface. Even when the wall superheat was as low as 2.2 °C, the sintered copper powder surface with the particle size of 110 μm and thickness of 0.6 mm could still be efficiently triggered to boiling. The heat transfer coefficient and CHF were significantly improved up to 247.71% and 255.15% compared with that of plain copper surface, respectively. However, with the thickness of porous layer increased from 0.6 mm to 0.9 mm, the maximum heat transfer coefficient for the enhanced surface with particle size of 30 μm went up to 136.01%, while the CHF value decreased by 92.52%. For 65 μm and 110 μm surfaces, the change of porous layer thickness had little effect on the heat transfer coefficient in the initial boiling stage, but presented the contrary influence trend at high heat flux conditions.

1. Introduction

In recent years, the heat dissipation of high heat flux electronic equipment has restricted the development of many emerging fields, such as information technology, high energy laser and radar, aerospace and so on [1]. Among many effective heat dissipation technologies for electronic equipment, phase change heat transfer technology is favored for its excellent uniform temperature performance and large heat transfer capacity. Pool boiling, as one of the efficient application modes of phase change heat transfer, has received extensive attention and research because of its remarkable advantages of rapid removal of huge heat flux and easy to be popularized in engineering [2]. However, the commonly used electronic coolants including dielectric liquids and some refrigerants suitable for electronic cooling have poor physical parameters such as low surface tension and low latent heat of vaporization, which have the negative effect on boiling heat transfer performance. At present, the reasonable modification of boiling surface was regarded as one of the important and feasible ways to improve the boiling heat transfer coefficient (HTC) and the critical heat flux (CHF) of electronic

* Corresponding author. Beijing Key Laboratory of Flow and Heat Transfer of Phase Changing in Micro and Small Scale, Beijing Jiaotong University, Beijing, 100044, China.
E-mail address: yinliaofei@bjtu.edu.cn (L. Yin).

https://doi.org/10.1016/j.csite.2022.102223
Received 31 May 2022; Received in revised form 16 June 2022; Accepted 20 June 2022
Available online 30 June 2022

coolants [3].

The use of machining, MEMS and NEMS techniques to fabricate surface micro/nano structures such as grooves, pins and pillar arrays to expand the heating area has been widely used to study the improvement of boiling heat transfer performance [4]. The influence of surface roughness was explored by El-Genk and Pourghasemi [5] where the surface roughness was produced by using emery paper of appropriate grit count, with HFE-7000 as the dielectric liquid, the maximum improvement of CHF and mean heat transfer coefficient could reach 39% and 2.32 times respectively. Another experiment done by El-Genk [6] also presented that under the surface roughness of $R_a = 1.44$ μm, the maximum heat transfer had a 150% enhancement compared to the untreated surface for more surface active nucleation sites provided by the roughness. Commonly used MEMS/NEMS processes such as lithography, etching and imprinting are effective methods to produce boiling strengthened surfaces. Wei et al. [7] fabricated surfaces of five different pin-fins geometries by dry etching technology, some steep boiling curves with small change in superheat were obtained in FC-72, which implied more nucleation sites were activated due to the highly-structured surfaces under the same wall superheat. Among all the surfaces, the surface with the thickness of 30 μm and fin height of 200 μm was recorded to have the best performance with its maximum heat flux about 4 times as large as that for a smooth chip. Analogous pin-fins structures in a microgravity environment were studied by Xue [8], compared to the normal gravity, the heat transfer haven't been seen an obvious variation, suggesting the offset effect might be provided by the capillary driving force. An enhancement of 40% on CHF and 60% on HTC in HFE-7100 was achieved by applying nano coatings (TiO_2) on substrates, Fan et al. [9] indicated that the improved bubble dynamics and efficient rewetting were the trigger of the high CHF and HTC. However, it was worth noting the machining of micro/nano structures on the curved surface or inner wall of tube of common heat exchangers was more complicated, and could even be lack of reliability and durability. In addition, for common metal heat transfer materials such as copper and aluminum, the large-size and large-scale applicability of MEMS and NEMS technology was also limited by many factors.

In order to be more general and convenient, many scholars were actively exploring the boiling heat transfer enhancement method of directly coating porous layer or porous material on the heated surface. Employing the powder flame spraying method, Dewangan et al. [10] studied the pool boiling heat transfer of copper coated tube in R-134a and R-600a, finding that compared with the uncoated tubes, the heat transfer coefficient was improved 0.99–2.1 times. Recently, with the electrically-assisted supersonic blowing technique being used, the nano-textured surfaces Sahu et al. [11] fabricated realized a 2–7 times heat fluxes enhancement than that of bare surfaces under the same surface superheat, which revealed the benefit of strong surface adhesion brought by ultrafine nanofiber sizes. El-Genk and Ali [12] coated copper powder onto substrate using electrochemical deposition method and performed the boiling experiments in PF-5060 and FC-72 respectively, in comparison with the plain surfaces, the values of mean heat transfer coefficient were reported to have an increase of 40%–70% in PF-5060 and more than 17 times boost in FC-72. A subsequent investigation on bubble dynamics by Furberg and Palm [13] showed that the improved heat transfer characteristics were due to the high nucleation bubble frequency density and more effective vapor escape paths provided by the interconnected porous network. Ho et al. [14] explored the possibility of modifying the pool boiling characteristics by SLM method. Microstructured surfaces of different configurations produced from $AlSi_{10}Mg$ powder all displayed significant enhancements on heat transfer performance, a 70% improvement in heat transfer coefficient and a 76% enhancement in CHF refer to the plain Al-6061 surfaces were observed. Such huge changes were resulted from the inherent surface grooves and cavities created from laser melting process. Manetti et al. [15] obtain a heat transfer augmentation of 100% and 82% respectively under moderated heat fluxes by using Cu and Ni metal foams, the high liquid reflux rate as well as the capillary wicking ability were considered to be the key factors that promoted the thermal conductivity of metal foam performance. To further evaluate pool boiling characteristics of metal foam, Li et al. [16] manufactured copper foams with and without channels while maintaining pore density, porosity and thickness unchanged. For refrigerant R141b, the HTC of copper foams with channels presented

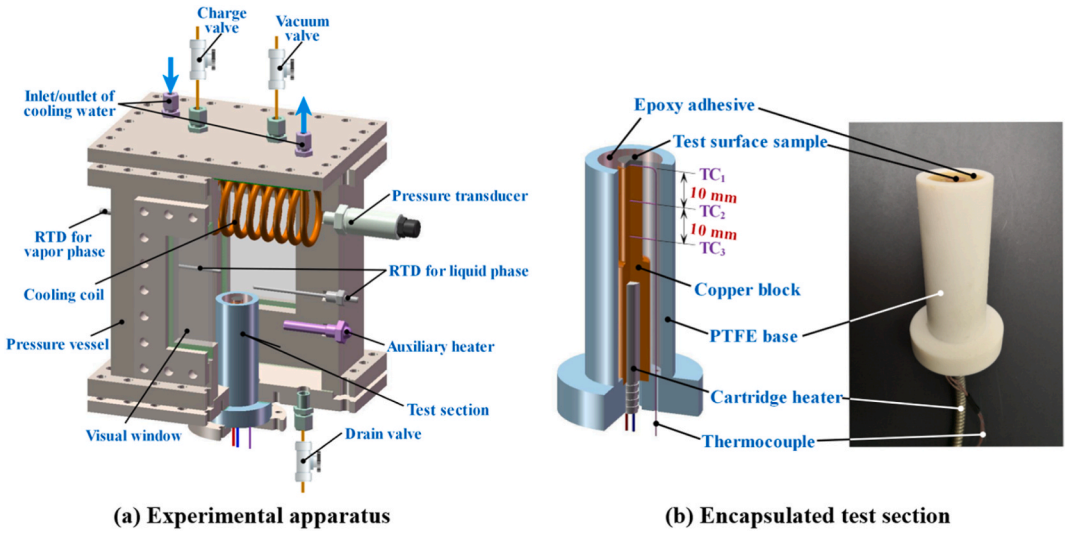

Fig. 1. Experimental facility of boiling apparatus.

an upward trend with heat flux increasing, but for copper foams without channels, a deteriorated phenomenon emerged under high heat flux. In order to obtain a better heat transfer performance, factors such as channel diameters, channel numbers should be considered as well. At present, surface modification techniques such as electrochemical deposition and chemical vapor deposition are expensive on the one hand, and there are also bottlenecks restricting engineering application on the other hand, especially the limitation of fabrication size and the effectiveness of pore structure. Though the method of sintered porous structure has the advantage of engineering popularization, it may also have some problems such as high contact thermal resistance, and the research on the relationship between pore characteristics and boiling heat transfer enhancement is insufficient.

In the present study, the heat transfer performance of sintered copper powder covered surfaces with different particle size and porous layer thickness was compared with the reference of plain copper surface. As the test fluid, R245fa was expected to be a potential electronic coolant. The evaluation of heat transfer performance was based on the variation tendency of boiling curve and heat transfer coefficient with wall superheat for different test surfaces. The visualization results of bubble behavior were used to assist in understanding and proving the dominant mechanism of heat transfer at different stages of the boiling process. In this experiment, the copper powder particle size and porous layer thickness were the key factors in the comparative analysis of this series of experiments.

2. Experiments

2.1. Experimental facility

Fig. 1(a) schematically shows the experimental apparatus suitable for studying pool boiling characteristics of low boiling point working fluids such as refrigerants and electronic coolants. The stainless-steel rectangular cavity and its upper and bottom cover plates were assembled as a closed pressure vessel. For capturing the bubble behavior during the boiling process, two symmetrical visualization windows were set on the front and rear walls, which were used for high-speed camera shooting and light source replenishment, respectively. The vacuum valve and charge valve installed on the upper cover plate were respectively connected with the vacuum pump and working fluid reservoir for vacuum treatment and test fluid infusion during the experimental preparation period. The cooling coil in the boiling vessel was connected with the chiller through the inlet and outlet of cooling water, so that the saturation pressure in the vessel can be controlled by condensing the steam in boiling process. The saturation temperature of the test liquid can be adjusted by the auxiliary heater inserted into the vessel through the side wall. Two pairs of PT1000 resistance temperature detectors (RTD) with the accuracy of ±0.15 °C were equipped to measure the temperature of vapor and liquid phase for test fluid respectively. The pressure in the vessel was monitored by the pressure transducer inserted into the vapor phase zone with the accuracy of ±0.25%. The drain valve was arranged on the lower cover plate to facilitate the recovery of working fluid after the end of the experiments. The packaged test section was inserted into the lower cover plate and then sealed with the pressure vessel through fastening parts.

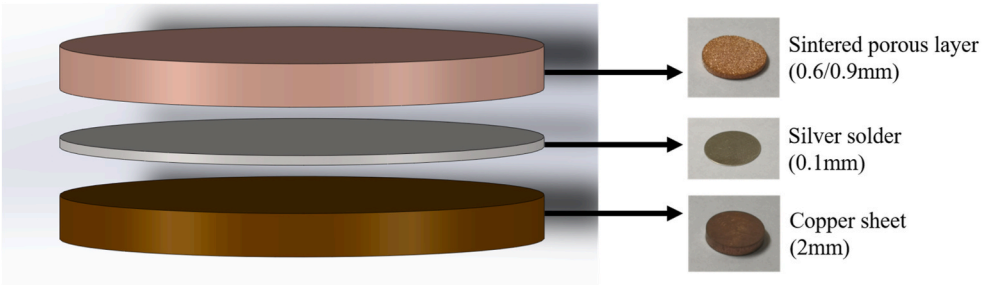

(a) The structure of test surface sample

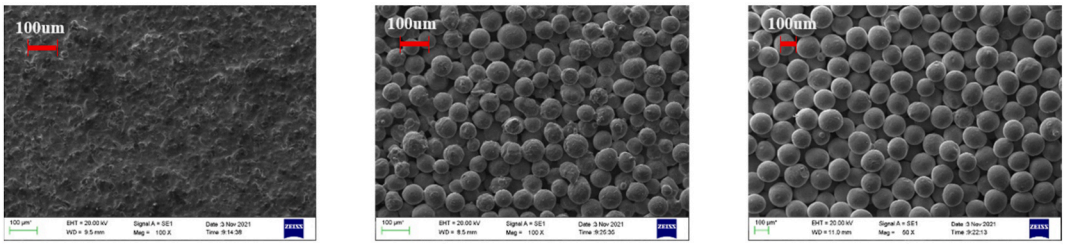

a) 30μm sintered copper powder surface

b) 65μm sintered copper powder surface

c) 110μm sintered copper powder surface

(b) Scanning electron microscope (SEM) photos of porous layers of sintered copper powder with different particle sizes

Fig. 2. Pictures of porous layers of sintered copper powder with different particle sizes.

Fig. 1(b) displayed the schematic and physical diagram of the specific structure of the encapsulated test section, which was mainly composed of heating module, heat insulation measures and the temperature measuring points. A cylindrical copper rod with a cartridge heater inserted at the bottom was used as the heating module, and its upper surface with the diameter of 10 mm in turn provided heat for test surface samples. In order to determine the effective heat flux and deduce the surface temperature of test surface samples, three temperature measuring points were set up on the upper surface of the copper rod and directly below the upper surface every 10 mm, where microholes ($D_m = 0.6$ mm, $L_m = 5$ mm) were machined to implant thermocouples. After installing the thermocouples, the microhole on the upper surface of copper rod was filled with copper solder and then flattened to guarantee the uniform heating towards the test surfaces sample as much as possible. The side microholes were filled with high thermal conductivity silicone grease ($k =$ 27.7 W/m K) to eliminate the gaps and enhance the axial heat flux uniformity. The heating module was placed in a PTFE base ($k = 0.26$ W/m K), and the gap between the two was pured and cured with low thermal conductivity epoxy adhesive ($k = 0.2$ W/m K). Thus, good thermal insulation conditions were created and the side boundary heating effect was basically eliminated. Besides, several micropores were also arranged at the bottom of PTFE base to facilitate the extension of thermocouple wires, which ensured the overall tightness of the test section in the pressure vessel and the convenience of measurement outside the vessel.

2.2. Test surface sample

As shown in Fig. 2(a), each of the test surface sample was composed of a copper sheet, a silver solder ($k = 410$ W/m K) pad and a sintered porous layer with the radius of 5 mm, which was consistent with the heating surface of the copper rod. The sintered porous layer with different copper powder size and coating thickness was obtained by sintering process with spherical copper powder particles, which were used as the boiling heat transfer enhancement layer on the plain surface of copper sheet. With the assistance of the diffusion welding process, the silver solder pad placed between the porous layer and the copper sheet was closely welded together, which not only increased the adhesion of the enhancement layer, but also greatly reduced the contact thermal resistance between the porous layer and the surface of the copper sheet. In order to ensure the accuracy of welding and prevent the oxidation of copper surface and copper powder, the test surface samples were embedded in the manufactured graphite mold for diffusion welding and protected by inert gas during the welding process. The porosity of the sintered porous layer for each specification was estimated by weighing six identical porous layer samples using the precision analytical balance and then comparing the weight with that of the solid samples of the same volume, and the average value was taken. The calculation method of permeability and equivalent pore diameter was referred to the recent research literatures [17–21]. Fig. 2(b) presented the scanning electron microscope (SEM) pictures of the sintered copper powder porous layers with the layer thickness of 0.9 mm/0.6 mm and particle size of 30 μm, 65 μm and 110 μm, respectively. The thickness of the copper sheet and the silver solder were 2 mm and 0.1 mm, respectively. The detailed parameters and characteristics of all the test surface samples involved in this study were summarized in Table 1 (see Table 2).

2.3. Experimental procedure

The refrigerant R245fa was used as the test fluid, which was suitable for electronic cooling applications because of its temperature-pressure correspondence. Before the start of each group of experiments, the pressure vessel needed to be vacuumed (lower than 10 mbar) and then injected into the test fluid to the scale line marked on the visual window, which was about 50 mm higher than the boiling surface. In order to avoid the influence of non-condensable gases in the test fluid and test surface samples, the refrigerant R245fa was boiled continuously for 1.5 h, while the CCD camera was adjusted to clearly capture the bubble behavior of the boiling process. During the experiments, the saturation temperature of the test liquid was always controlled at about 20 °C with the deviation less than ±1.5 °C. The subcooled state of the test fluid was necessary and limited to less than 2 °C, thus ensuring that the test fluid was as close to saturation boiling as possible while avoiding cavitation phenomenon. Each group of boiling experiment was carried out according to the established heat flux interval and the relevant data were recorded in the corresponding steady state. In the initial stage, the heat flux interval was set to 1 kW/m^2 to facilitate the capture of ONB point. With the increase of heat flux, the interval gradually transited from 1 kW/m^2 to 5 kW/m^2 until the boiling crisis (CHF point) was reached.

3. Data reduction

3.1. Heat transfer

The pool boiling heat transfer coefficient of R245fa for the test sample surfaces could be calculated according to the Newton's cooling law as follows:

Table 1
Characteristics of test surface samples.

Surface type	Surface number	Roughness	Effective capillary radius	Thickness	Pore diameter	Porosity	Permeability
		μm	μm	mm	μm	%	K/m^2
Plain copper surface	S–P	Ra 0.375					
Sintered powdered copper surface	S-0.9-A	On S–P	8.3	0.9	30	36.56%	8.3×10^{-13}
	S-0.9-B	On S–P	34.5	0.9	65	49.07%	8.9×10^{-12}
	S-0.9-C	On S–P	106	0.9	110	67.83%	2.3×10^{-11}
	S-0.6-A	On S–P	8.3	0.6	30	36.56%	8.3×10^{-13}
	S-0.6-B	On S–P	34.5	0.6	65	49.07%	8.9×10^{-12}
	S-0.6-C	On S–P	106	0.6	110	67.83%	2.3×10^{-11}

Table 2
Uncertainties of experimental parameters.

Measured		Calculated	
Parameter	Uncertainty	Parameter	Uncertainty
L	±0.005 mm	q_{eff}	±0.78–7.10%
T (K-type/RTD)	±0.10 °C/±0.15 °C	T_s	±0.13–1.40%
p	±0.25%	h_b	±1.17–8.20%
Q	±0.50%		

$$h = \frac{q_{eff}}{T_s - T_{sat}} \tag{1}$$

where, q_{eff} represented the effective heat flux passing through the test surface samples. The sides of heating module as well as the test surface sample were well thermal insulated and the total heat loss of the test section within all experimental conditions was less than 4.53% compared to the heating power. Thus, the effective heat flux could be derived based on one-dimensional Fourier's law along the axial direction of the test section and given by Eq. (2) as follows:

$$q_{eff} = -k \cdot \frac{d_T}{d_x} \tag{2}$$

where, k was the thermal conductivity of copper; ΔT and ΔL denoted the temperature difference and vertical distance between the temperature measuring points along the copper rod, respectively. The temperature measurements of the three thermocouples (TC_3 to TC_1) basically presented a linear regression trend in the range of experimental conditions in this study, and the R^2 values were all greater than 99%. Therefore, the heat loss of the copper rod between the measuring points of TC_3 to TC_1 could be ignored. To further improve the calculation accuracy at low heat flux, the temperature of TC_3 and TC_1 was more suitable for deriving effective heat flux than TC_2 and TC_1, thus, ΔT and ΔL could be expressed as $\Delta T = T_3\text{-}T_1$ and $\Delta L = L_3\text{-}L_1$.

T_s represented the temperature of boiling surface, which was uniformly based on the upper surface of the copper sheet base for all test surface samples and could also be determined according to Fourier's law as follows:

$$T_s = T_1 - q_{eff} \cdot \left(\frac{L_1}{k_{Cu}} + \frac{L_{grease}}{k_{grease}} + \frac{L_{sample}}{k_{Cu}} \right) \tag{3}$$

where, k_{grease} and L_{grease} represented the thermal conductivity and thickness of thermal conductive silicone grease, which were estimated to be 16 W/m K and 0.05 mm, respectively. L_{sample} referred to the thickness of the copper sheet base of test surface samples (2 mm). The saturation temperature T_{sat} for the test fluid of R245fa was directly obtained from the averaged measurement values from RTDS in the liquid phase in the pressure vessel, which avoided the indirect error caused by querying the saturation temperature with the corresponding pressure value though the software.

3.2. Uncertainty analysis

The uncertainties related to the derived experimental data could be analyzed according to the method proposed by Moffat [22] and recommended in similar research literatures [23,24], given by:

$$U_y = \left[\sum_{i=1}^{n} \left\{ \left(\frac{\partial y}{\partial x_i} \right) U x_i \right\}^2 \right]^{\frac{1}{2}} \tag{4}$$

where, U_{xi} = uncertainty associated with x_i.

Thus, the uncertainty of the effective heat flux could be calculated by:

$$\frac{\delta q_{eff}}{q_{eff}} = \sqrt{\left(\frac{\delta T_1}{\Delta T_{13}} \right)^2 + \left(\frac{\delta T_3}{\Delta T_{13}} \right)^2 + \left(\frac{\delta L_{13}}{L_{13}} \right)^2} \tag{5}$$

where, δT_1 and δT_3 were represented by the accuracies of the calibrated thermocouples and RTDs (±0.10 °C and ±0.15 °C) respectively. δL_{13} could be determined by the machining accuracy of ±0.005 mm.

The uncertainty corresponded to the surface temperature of the test surface samples was given by Eq. (6), in which the uncertainty of thermal conductivity of copper was also considered with the reasonably estimated value of ±1%.

$$\frac{\delta T_s}{T_s} = \sqrt{\left(\frac{\delta T_1}{T_s} \right)^2 + \left(\frac{L_{s1}}{k_{Cu}} \cdot \frac{\delta q_{eff}}{T_s} \right)^2 + \left(\frac{q_{eff}}{k_{Cu}} \cdot \frac{\delta L_{S1}}{T_s} \right)^2 + \left(\frac{q_{eff} L_{s1}}{k^2{}_{Cu}} \cdot \frac{\delta k_{Cu}}{T_s} \right)^2} \tag{6}$$

Then, the uncertainty of the pool boiling heat transfer coefficient was as follows:

$$\frac{\delta h_b}{h_b}=\sqrt{\left(\frac{\delta q_{eff}}{q_{eff}}\right)^2+\left(\frac{\delta T_s}{T_s-T_{sat}}\right)^2+\left(\frac{\delta T_{sat}}{T_s-T_{sat}}\right)^2} \tag{7}$$

Considering the accuracy of the testing instruments and the influence of the range of experimental conditions, the measured and calculated uncertainties of experimental parameters were all summarized Table 1.

4. Results and analysis

4.1. ONB (onset nuclear boiling) analysis

Fig. 3 displayed the effective heat flux versus the wall superheat near the ONB point for all test surface samples. For the test fluid of R245fa, the wall superheat at the ONB point of the plain copper surface exceeded 30 °C and the corresponding heat flux reached about 50 kW/m^2. But the boiling of all sintered copper powder surfaces in this study could be triggered under the condition that the wall superheat did not exceed 7 °C with further low heat flux. This was due to the fact that the porous layer of each test surface sample provided sufficient effective nucleation sites at the initial boiling time.

After the onset of nucleate boiling, the plain copper surface showed a typical ONB point trigger phenomenon, and the wall superheat dropping as high as 14.3 °C with the increase of heat flux. However, all the porous layer covered surfaces did not present the falling characteristic of wall superheat. Among them, the sintered copper powder surfaces of S-0.6-B (65 μm) and S-0.6-C (110 μm) particle size have the ONB points as low as about 3 °C, and the rise of heat flux in the initial boiling stage has little effect on their wall superheats. But for the surface S-0.6-A (30 μm), not only the ONB point lagged obviously, but also the slope of heat flux with wall superheat was significantly smaller than that of the surfaces S-0.6-B and S-0.6-C. According to the visualization results shown in Fig. 4, the nucleation state of surface S-0.6-A at the initial boiling time was obviously weaker that the other two enhanced surfaces, and the bubble detachment diameter was also relatively small. This means that the number of initial effective nucleation sites on surface S-0.6-A was small, and at the same time, the pore size was too small, which also increased the bubble detachment resistance, resulting in the negative effect of initial boiling of R245fa.

In addition, it could also be seen from Fig. 3 that thickness of the porous layer in the present study had no obvious effect on the onset of nucleate boiling of the test fluid R245fa, since the boiling surfaces of each copper powder size specification could provide the required sufficient effective nucleation sites no matter the thickness of 0.6 mm or 0.9 mm, which was regarded as the main decisive factor at the initial moment of boiling.

4.2. Effect of copper powder size of sintered porous layer

In order to analyze the effect of pore characteristics on heat transfer performance, the boiling curve and heat transfer coefficient versus wall superheat for the sintered copper powder surfaces with different particle sizes were displayed in Fig. 5(a) and Fig. 5(b), respectively. The corresponding characteristics of plain copper surface were taken as the reference since the porous layer of enhanced boiling surfaces were directly welded on it.

For characteristics of heat transfer coefficient, it could be seen that the changing trend for the enhanced surface with the particle size of 30 μm was similar to that of the plain copper surface, while the variation curve for the enhanced surface S-0.6-B with the particle size of 65 μm closely resembled that of the surface with the particle size of 110 μm. Within the present test conditions, the maximum heat transfer coefficients of the three sintered copper powder surfaces were increased to 136.96%, 240.45% and 248.12% respectively compared to the copper plain one as shown in Fig. 5(b). Compared with the plain copper surface, the heat transfer coefficient of surface S-0.6-A increased with a more rapid rate at the initial moment until it reached the inflection point at the heat flux of 286.43 kW/m^2,

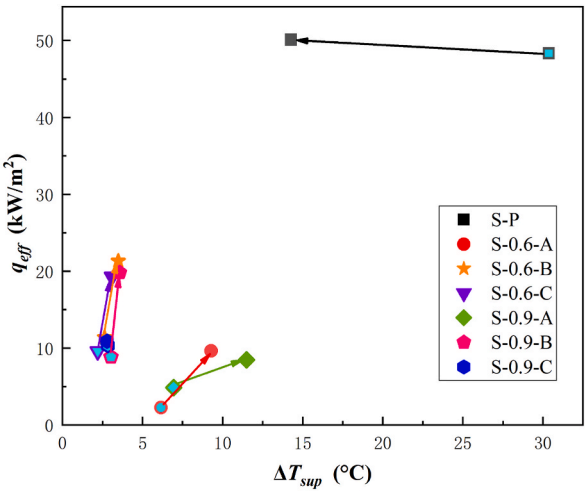

Fig. 3. ONB points for different test surfaces.

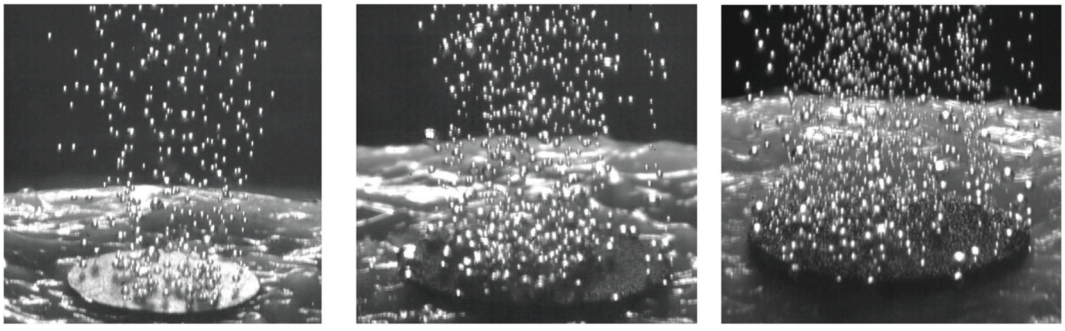

(a) surface S-0.6-A (b) surface S-0.6-B (c) surface S-0.6-C

Fig. 4. Visual image at ONB point.

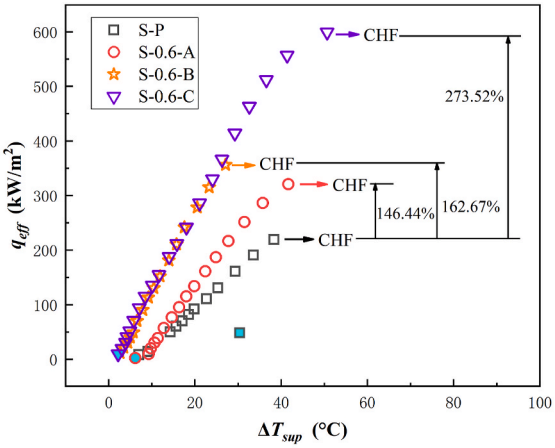

(a) Boiling curve

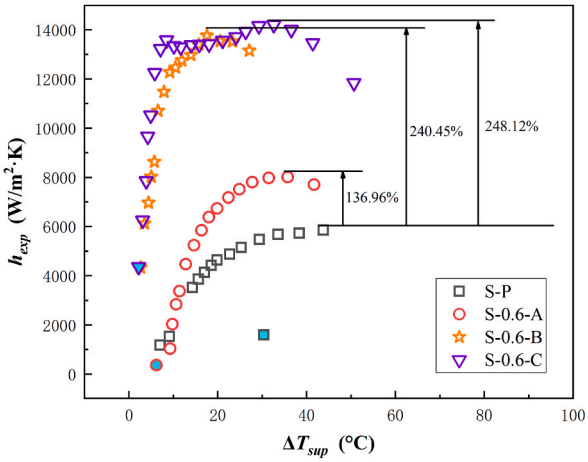

(b) Heat transfer coefficient

Fig. 5. Nucleate pool boiling curves and heat transfer coefficient of plain copper surfaces with different pore size.

where the number of activated nucleation sites was nearly saturated and the intense coalescence of bubbles also offset the benefit of bubble departure under that higher heat flux. Thus, the heat transfer coefficient began to decrease. For the surfaces of S-0.6-B and S-0.6-C, the heat transfer coefficients were relatively high at the beginning of boiling. With the wall superheat from 2 °C to 10 °C, the heat transfer coefficient of the above two surfaces increased sharply from 4000 kW/m^2·K to about 13,000 kW/m^2·K, which was much larger than that of surface S-0.6-A and could also be intuitively reflected in the boiling curve, with obvious smaller slope in Fig. 5(a). In this boiling stage, more and more effective nucleation sites in the porous layer were continuously activated, because the larger particle size expanded the range of effective nucleation size as well as the number. After that, the increasing trend of the heat transfer coefficient versus wall superheat for surface S-0.6-B obviously slowed down. Until the moment when the effective heat flux $q > 241.89$ kW/m^2, the heat transfer coefficient began to decline due to the reasons similar to that of enhanced surface with particle size of 30 μm.

However, for the surface S-0.6-C with 110 μm particle size, with the increase of effective heat flux, there was a stagnation point at $q = 114.83$ kW/m^2 in the growth tendency of the heat transfer coefficient. This meant that the effective nucleation sites formed by the pores of copper powder had been fully activated. After that point, the increasing trend of heat transfer coefficient was significantly suppressed until the heat flux exceeded 241.84 kW/m^2, and the heat transfer coefficient increased slightly again. The most likely reason was that the nucleation sites existing on the surface of copper powder with large particle size was activated under high heat flux, resulting in such a secondary activation and nucleation phenomenon. This could also be illustrated in Fig. 5(a), where the boiling curve of surface S-0.6-C with 110 μm particle size still kept a good upward trend after the surface S-0.6-B reached the critical heat flux, although the previous two boiling curves almost coincided.

As shown in Fig. 6, the visualization results of pool boiling on surface S-0.6-A, S-0.6-B and S-0.6-C was selected as the examples to illustrate the bubble behavior. With the increase of heating power, the volume and number of bubbles on the surface gradually increased. When a large number of bubbles gathered near the surface, they would connect with each other to form a large bubble.

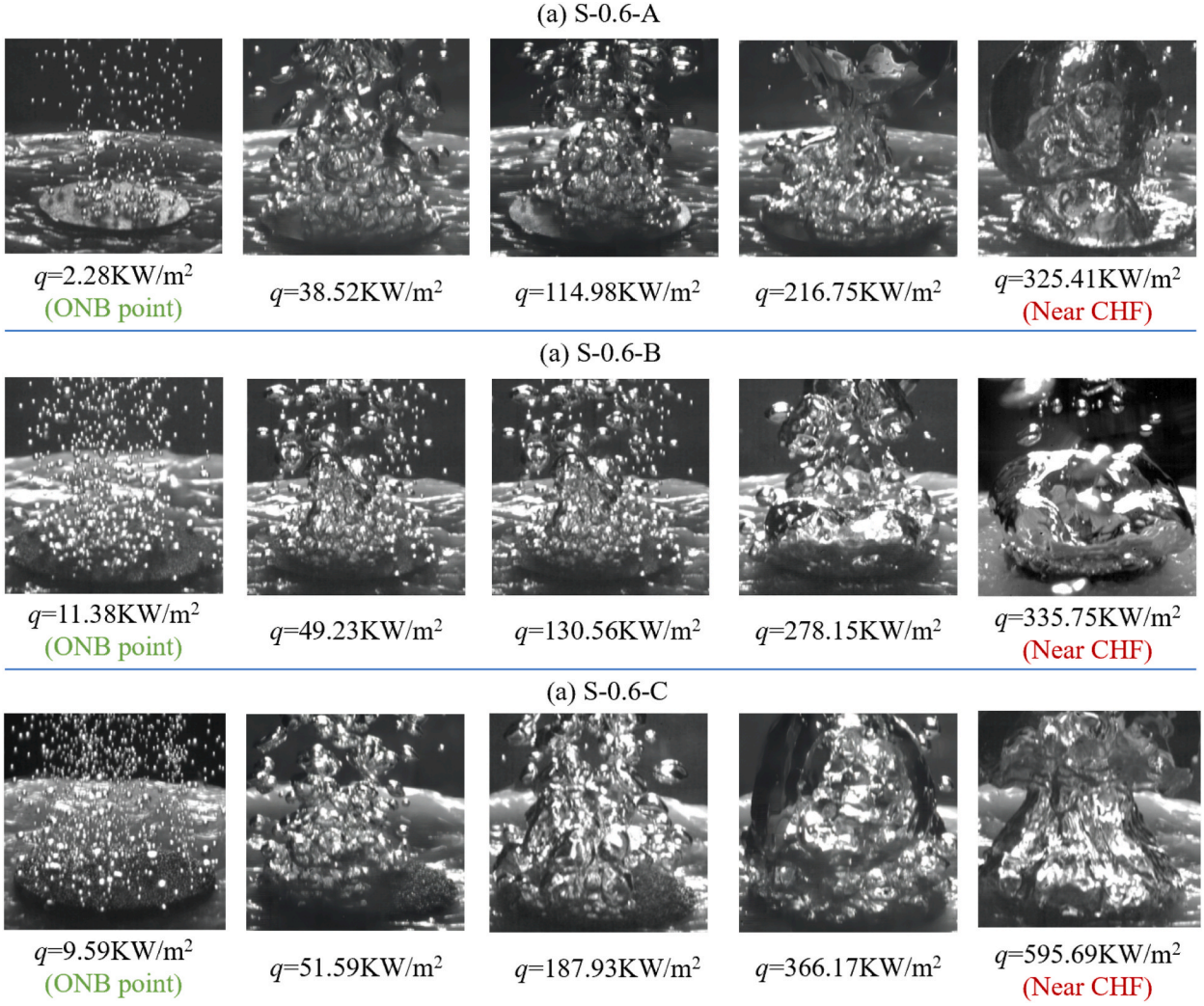

Fig. 6. Visualized nucleate pool boiling process on sintered copper powder surfaces of S-0.6-A, S-0.6-B, S-0.6-C.

Compared with small bubbles that are prone to disengage, these large bubbles took longer time to separate and covered a large part of heating area. In addition, since the vapor phase film near the surface formed a great thermal resistance, the heat transfer performance of the surface would be significantly reduced, and the heat flux at this time was close to that of CHF, as displayed in Fig. 7 for S-0.6-A and S-0.9-B. Besides, as shown in Fig. 5(a), the critical heat flux for the three sintered copper powder surfaces (30 μm, 65 μm and 110 μm particle size) increased to about 146.44%, 162.67 and 273.52% compared to the plain copper surface, respectively. From the point of view of particle size, the improvement of CHF value mainly depended on the relative force magnitude and dynamic balance effect of bubble detachment resistance, liquid reflux resistance and capillary wicking in the porous layer under the condition of high heat flux. Within the experimental scope of this study, the decrease of vapor and liquid phase flow resistance in porous layer caused by the increase of pore size, i.e., the increase of particle size, was the main factor conducive to the enhancement of CHF.

4.3. *Effect of porous layer thickness of sintered copper powder surface*

Due to the limitation and influence of copper powder sintering process and porous layer welding process, after many attempts under laboratory conditions, the contrast thickness of sintered copper powder surfaces with different particle size was 0.6 mm and 0.9 mm. The porous layers of these specification presented almost uniform and stable material appearance. According to the previous analysis, the boiling heat transfer characteristics of surface S-0.6-B and S-0.6-C were obviously different from those of surface with particle size of 30 μm. Thus, the sintered copper powder surface of 30 μm particle size with different thickness were compared separately as shown in Fig. 8, while the surfaces of 65 μm and 110 μm particle sizes were compared together given by Fig. 9. As shown in the variation of heat transfer coefficient in Fig. 8(b), for the sintered porous layer with small particle size of 30 μm, the corresponding heat transfer coefficient of surface S-0.6-A with the thickness of 0.6 mm was always higher than that of surface S-0.9-A with the thickness of 0.9 mm regardless of the effective heat flux. The maximum heat transfer coefficient of S-0.6-A was improved to 136.01% compared to that of surface S-0.9-A, which was attributed to the rise of thermal resistance. Based on the fact of small pore size caused by small particle size copper powder, the additional thickness would lead to greater nucleation resistance and more difficult bubble growth and detachment effects as well as the increased thermal resistance. These factors obviously play a more dominant role in the enhancement of heat transfer performance than the benefits of the increase in the number of nucleation sites within small and limit sizes.

However, the increase of the thickness of the porous layer with 30 μm particle size led to the increase in the number of nucleation sites with not only small pore size but also the limited size range of the pore size. Although the internal flow resistance of the porous layer increased, it also provided the potential activable nucleation basis as the favorable offset under high heat flux conditions. Therefore, the critical heat flux of surface S-0.9-A with thickness of 0.9 mm was 108.09% higher than that of surface S-0.6-A with thickness of 0.6 mm as shown in Fig. 8, For the sintered copper powder surfaces with particle size of 65 μm and 110 μm, the thickness of porous layer had no significant effect on the boiling heat transfer coefficient before reaching the turning point heat flux at about 114 kW/m^2. Although the thicker porous layer increased the vapor and liquid flow resistance, the pore size of the sintered surface of 65 μm and 110 μm copper powder particles was relatively large, and the size range of the effective nucleation sites was wider, so it was easier to be activated, and the increase in porous layer thickness also provided a richer number of nucleation sites. Thus, the thickness factor

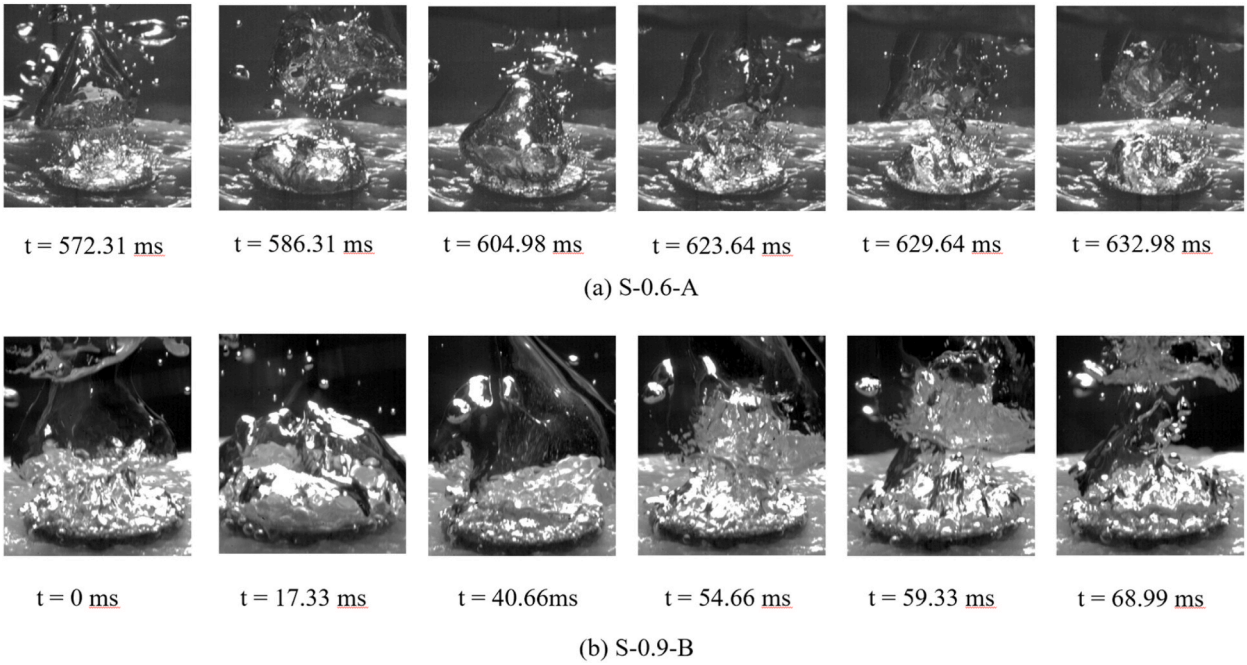

Fig. 7. Visualized CHF process on surface S-0.6-A and S-0.9-B.

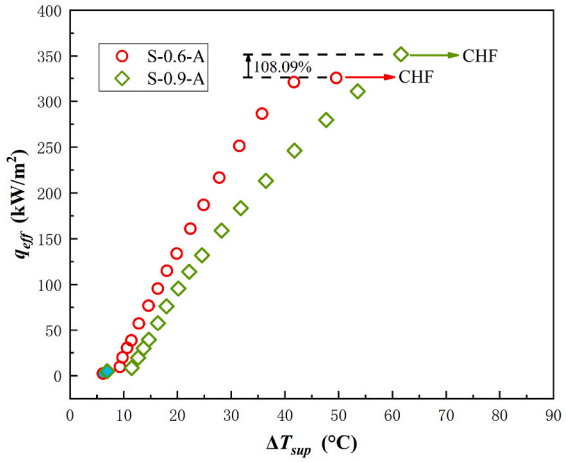

(a) Boiling curves

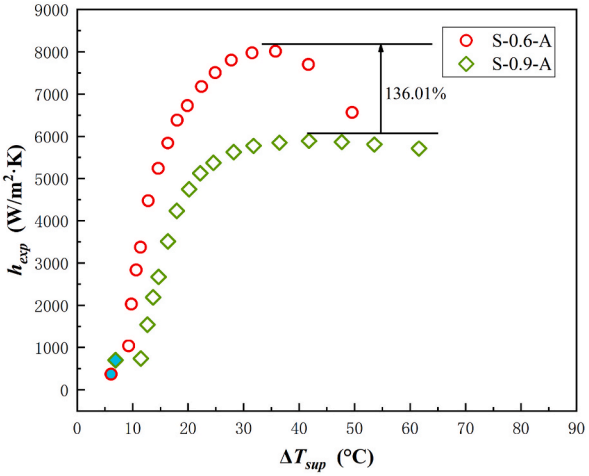

(b) Heat transfer coefficient

Fig. 8. Nucleate pool boiling curves and heat transfer coefficient of plain copper surfaces with different layer thickness.

had little effect on the heat transfer performance in the initial boiling stage of these two particle size specification surfaces.

It was worth noting that there were some differences in the effect of porous layer thickness on boiling heat transfer characteristics under the condition of high effective heat flux for enhanced surfaces with particle size of 65 μm and 110 μm. The heat transfer coefficient of surface S-0.9-B with the thicker porous layer of 0.9 mm was higher than that of surface S-0.6-B, while that of surface S-0.6-C with the thinner porous layer of 0.6 mm was higher than that of surface S-0.9-C at higher heat flux. Thus, due to the inertia of heat transfer, the critical heat flux for thicker porous layer with 65 μm copper powder particle size increased to 127.53%, while the corresponding value decreased 88.62% for the thicker one with 110 μm as shown in Fig. 9(a). The most likely reason for this anomaly was that the pore size of the 110 μm copper powder sintered layer was larger, so the proportion of liquids with low thermal conductivity in the porous structure was higher, and the increase of thickness would be more sensitive to the increase of the thermal resistance of the whole porous layer compared with the enhanced surface of 65 μm particle size.

5. Conclusion

In this study, the nucleate pool boiling experiments of R245fa on plain copper surface and sintered copper powder surface were carried out. The enhancement effect of copper powder particle size and porous layer thickness on boiling heat transfer performance were analyzed. The main conclusions were summarized as follows:

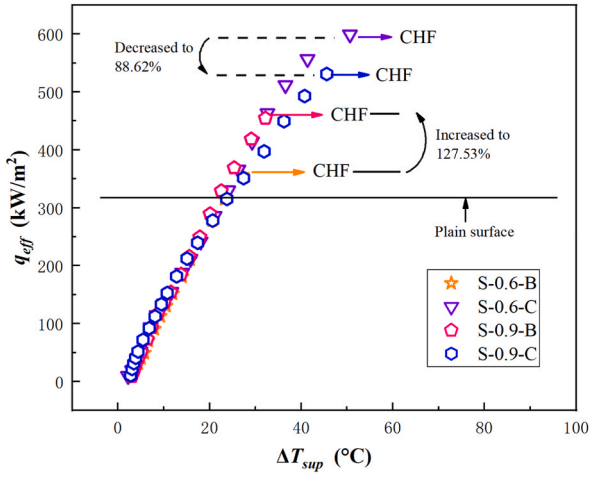

(a) Boiling curves

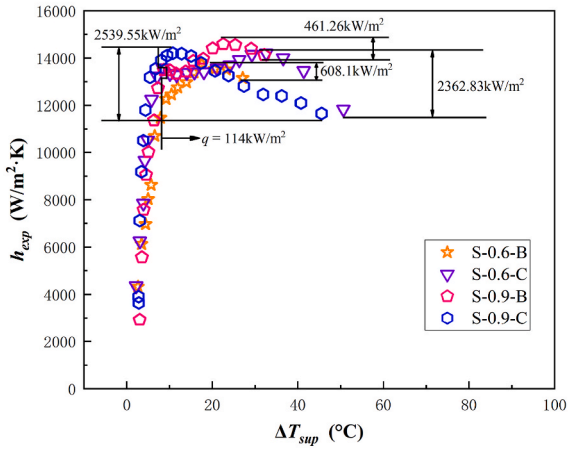

(b) Heat transfer coefficient

Fig. 9. Nucleate pool boiling curves and heat transfer coefficient of plain copper surfaces with different layer thickness.

(1) Compared to the plain copper surface with wall superheat higher than 30 °C at ONB point, the wall superheats required for all test sintered copper powder surfaces were lower than 7 °C. The trigger temperature of boiling initiation for the enhanced surface with particle size of 110 μm and thickness of 0.6 mm was even lower than 2.2 °C.

(2) Taking the plain copper surface as the reference, the maximum heat transfer coefficient and CHF value increased to 240.45% and 162.67% for sintered copper powder surface with particle size of 65 μm and 248.12% and 273.52% with 110 μm respectively. For 30 μm copper power sintered porous surface with small size range of effective nucleation sites, the further improvement of heat transfer performance was limited and the maximum heat transfer coefficient and CHF value only increased to 136.96% and 146.44%, respectively.

(3) For 30 μm copper powder sintered porous surface, the maximum heat transfer coefficient with the porous layer thickness of 0.6 mm was 136.01% higher than that of 0.9 mm, while the CHF value reduced to 92.52% rather than improvement. As for the 65 μm and 110 μm surfaces, increasing porous layer thickness from 0.6 mm to 0.9 mm had little effect on the rapid nucleation stage during the initial boiling process, but the enhancement effect gradually presented an opposite trend at high effective heat flux conditions.

Author statement

Chao Dang: Conceptualization, Investigation, Writing - Original Draft, Writing - Review & Editing.
Lingyun Pan: Investigation, Validation, Data Curation.
Ruiqi Min: Investigation, Validation, Data Curation.
Liaofei Yin: Conceptualization, Investigation, Project planning.

Yi Ding: Validation, Data Curation.
Hongwei Jia: Validation, Data Curation.

Conflicts of interest

We wish to confirm that there are no known conflicts of interest associated with this publication and there has been no significant financial support for this work that could have influenced its outcome.

We confirm that the manuscript has been read and approved by all named authors and that there are no other persons who satisfied the criteria for authorship but are not listed. We further confirm that the order of authors listed in the manuscript has been approved by all of us.

We confirm that we have given due consideration to the protection of intellectual property associated with this work and that there are no impediments to publication, including the timing of publication, with respect to intellectual property. In so doing we confirm that we have followed the regulations of our institutions concerning intellectual property.

Declaration of competing interest

The authors declare that they have no known competing financial interests or personal relationships that could have appeared to influence the work reported in this paper.

Acknowledgments

This research was supported by the National Natural Science Foundation of China (No. 52106069), the Beijing Natural Science Foundation (No. 3214054) and the Fundamental Research Funds for the Central Universities (No. 2022RC024).

References

[1] J. Lee, I. Mudawar, Low-temperature two-phase microchannel cooling for high-heat-flux thermal management of defense electronics, IEEE Trans. Compon. Packag. Technol. 32 (2009) 453–465.
[2] I. Mudawar, Assessment of high-heat-flux thermal management schemes, Components & Packaging Technologies IEEE Transactions on 24 (2001) 122–141.
[3] D.E. Kim, D.I. Yu, D.W. Jerng, et al., Review of boiling heat transfer enhancement on micro/nanostructured surfaces, Exp. Therm. Fluid Sci. 66 (2015) 173–196.
[4] M. Shojaeian, A. Kosar, Pool boiling and flow boiling on micro- and nanostructured surfaces, Exp. Therm. Fluid Sci. 63 (2015) 45–73.
[5] M.S. El-Genk, M. Pourghasemi, Experimental investigation of saturation boiling of HFE-7000 dielectric liquid on rough copper surfaces, Therm. Sci. Eng. Prog. 15 (2019), 100428.
[6] M.S. El-Genk, A. Suszko, Saturated nucleate boiling and correlations for PF-5060 dielectric liquid on inclined rough copper surfaces, J. Heat Tran. 136 (2014), 081503.
[7] J. Wei, L. Guo, H. Honda, Experimental study of boiling phenomena and heat transfer performances of FC-72 over micro-pin-finned silicon chips, Heat Mass Tran. 41 (2005) 744–755.
[8] Y. Xue, J. Zhao, J. Wei, et al., Experimental study of nucleate pool boiling of FC-72 on micro-pin-finned surface under microgravity, Int. J. Heat Mass Tran. 63 (2013) 425–433.
[9] S. Fan, W. Tong, F. Duan, Nucleate pool boiling heat transfer enhancement in saturated Novec 7100 using titanium dioxide nanotube arrays, Int. Commun. Heat Mass Tran. 122 (2021), 105166.
[10] A.K. Dewangan, A. Kumar, R. Kumar, Experimental study of nucleate boiling heat transfer of R-134a and R-600a on thermal spray coating surfaces, Int. J. Therm. Sci. 110 (2016) 304–313.
[11] R.P. Sahu, S. Sinha-Ray, S. Sinha-Ray, et al., Pool boiling on nano-textured surfaces comprised of electrically-assisted supersonically solution-blown, copper-plated nanofibers: experiments and theory, Int. J. Heat Mass Tran. 87 (2015) 521–535.
[12] M.S. El-Genk, A.F. Ali, Enhanced nucleate boiling on copper micro-porous surfaces, Int. J. Multiphas. Flow 36 (10) (2010) 780–792.
[13] R. Furberg, B. Palm, Boiling heat transfer on a dendritic and micro-porous surface in R134a and FC-72, Appl. Therm. Eng. 31 (16) (2011) 3595–3603.
[14] J.Y. Ho, K.K. Wong, K.C. Leong, Saturated pool boiling of FC-72 from enhanced surfaces produced by Selective Laser Melting, Int. J. Heat Mass Tran. 99 (2016) 107–121.
[15] L.L. Manettia, G. Ribatskib, R.R. Souzaa, et al., Pool boiling heat transfer of HFE-7100 on metal foams, Exp. Therm. Fluid Sci. 113 (2020), 110025.
[16] T. Li, X. Wu, Q. Ma, Pool boiling heat transfer of R141b on surfaces covered copper foam with circular-shaped channels, Exp. Therm. Fluid Sci. 105 (2019) 136–143.
[17] D. Huang, L. Jia, Study on capillary properties of liquid absorption core of sintered copper powder, J. Eng. Thermophys. 42 (2021) 494–503.
[18] D. Huang, L. Jia, H. Wu, et al., Experimental investigation on the vapor chambers with sintered copper powder wick, J. Therm. Sci. 30 (2021) 1938–1950.
[19] H.S. Ahn, G. Park, M.K. Ji, et al., The effect of water absorption on critical heat flux enhancement during pool boiling, Exp. Therm. Fluid Sci. 42 (2012) 187–195.
[20] M.M. Rahman, E. Ölçeroglu, M. McCarthy, Role of wickability on the critical heat flux of structured superhydrophilic surfaces, Langmuir 30 (2014) 11225–11234.
[21] Z. Cao, Z. Wu, A.D. Pham, et al., Pool boiling of HFE-7200 on nanoparticle-coating surfaces: experiments and heat transfer analysis, Int. J. Heat Mass Tran. 133 (2019) 548–560.
[22] R.J. Moffat, Describing the uncertainties in experimental results, Exp. Therm. Fluid Sci. 1 (1988) 3–17.
[23] D. Liu, Y. Li, A. Hu, Visualization of boiling heat transfer on copper surface with different wettability, J. Therm. Sci. (2022), https://doi.org/10.1007/s11630-022-1599-4.
[24] N. Xu, H. Jiang, L. Peng, et al., Dynamic analysis of bubble attachment and sweeping on microwire in subcooled nucleate pool boiling, J. Therm. Sci. 30 (2021) 1842–1858.

International Journal of Thermal Sciences 187 (2023) 108183

Contents lists available at ScienceDirect

International Journal of Thermal Sciences

journal homepage: www.elsevier.com/locate/ijts

Saturated pool boiling heat transfer enhancement of R245fa based on the surface covered by sintered copper powder with and without nanostructure

Chao Dang [a,*], Ruiqi Min [a], Lingyun Pan [a], Liaofei Yin [a,b], Zhiqiang Zhang [a], Yanxin Hu [c]

[a] Beijing Key Laboratory of Flow and Heat Transfer of Phase Changing in Micro and Small Scale, Beijing Jiaotong University, Beijing, 100044, China
[b] Key Laboratory of Thermal Science and Power Engineering of Ministry of Education, Department of Energy and Power Engineering, Tsinghua University, Beijing, 100084, China
[c] School of Materials and Energy, Guangdong University of Technology, Guangzhou, 510006, China

ARTICLE INFO

Keywords:
Pool boiling
Porous layer
Surface modification
Heat transfer enhancement
Refrigerant

ABSTRACT

The pool boiling characteristics on the enhanced surfaces with sintered copper powder coatings with and without nano-treatment were experimentally investigated. Three kinds of enchanted surfaces formed by sintered porous layers with copper powder particles and their further nano-treated surfaces were adopted as the test surfaces. The thermal oxidation process was used to form nanostructures with super hydrophilic characteristic on the surface of sintered copper particles. Refrigerant R245fa was selected as the test fluid due to the potential the application in electronic cooling field. The saturation temperature of boiling experiments was maintained about 20 °C. The result showed that the boiling heat transfer performance was effectively improved by coating sintered copper powder porous layer on the plain copper surface, and the maximum heat transfer coefficient and CHF value enhancement could reach 151% and 160% of the plain one, respectively. The enhanced surfaces no matter with or without nano-treatment could trigger the nucleation process at the wall superheats lower than 12 °C rather than the value as high as 30 °C for plain copper surface. After nano-treatment, the heat transfer enhancement for sintered porous surfaces was further improved at medium and low heat flux, where the bubble nucleation or detachment remained robust. The CHF peaked as 140% of untreated surface, while the heat transfer coefficient increased to 108% at most.

1. Introduction

Nowadays, with the rapid development of integrated circuits together with miniaturization trend of electronic equipment, the heat dissipation load of electronic equipment continued to break through the limit [1]. The high heat flux characteristic would not only affect the operating performance and effective life of the equipment, but also restrain the performance upgrade brought about by the iteration of technology update, which directly hindered the production cost and economic benefits of emerging industries [2]. Therefore, the development and intervention of efficient heat dissipation technology were urgently needed in advanced manufacturing fields such as radar, information and communication, electromagnetic power, aerospace and so on. At present, the two-phase cooling scheme based on phase change boiling heat transfer were widely concerned for its ability to make full use of the latent heat of the coolants, and achieved the very high effective heat dissipation capacity while maintaining a good operating temperature range of the equipment [3]. In particular, considering current-carrying electronics and power equipment, the choice of coolant in cooling system considerations must be inert and dielectric, such as electronic fluorination liquids or refrigerants. However, the relatively poor thermophysical properties, high air solubility and extremely small surface tension have negative effects on boiling heat transfer. Therefore, focusing on the corresponding boiling heat transfer enhancement technology was one of the important issues to keep up with the heat dissipation growth of advanced electronic equipment [4].

The surface modification method for the fabrication of micro/nanostructures was widely used idea of boiling surface heat transfer enhancement. Many research topics were focused on the use of selective laser melting (SLM), electrical discharge machining (EDM), micro-electro-mechanical system (MEMS), nano-electro-mechanical system (NEMS) and other technologies to fabricate micro-fins, microarrays and other microstructures on the heat transfer surface. At the same time, anodic oxidation, e-beam evaporator and electrostatic deposition were

* Corresponding author.
E-mail address: dangchao@bjtu.edu.cn (C. Dang).

https://doi.org/10.1016/j.ijthermalsci.2023.108183
Received 22 September 2022; Received in revised form 9 December 2022; Accepted 20 January 2023

also used to further treated the microstructure to obtain micro-nanocomposite structures. Bregar and Vodopivec [5] found that samples with a single laser weaving nucleation site can decompose isolated bubbles, and graphene oxide deposition will lead to higher nucleation temperature, resulting in larger detachment diameter and longer growth time of bubbles. Ho and Wong [6] made micro-fins and micro-cavities surfaces from $AlSi_{10}Mg$ base powder using SLM technology. The CHF value and heat transfer coefficient in the pool boiling test of FC-72 were increased by 76% and 89% respectively, and the enhancement was owing to the inherent grooves and holes on the surface from laser melting. Ferjančič and Može [7] used laser textured stainless steel surface combined with hydrophobic coating to prepare many types of surfaces with circular spots with capillary length intervals of different diameters. All the modified surfaces acquired increased CHF, 36%–73%" at saturation and 34%–65%" at 12K supercooling. Jones et al. [8] studied the effect of surface roughness on pool boiling heat transfer of FC-77 with the polished surfaces (Ra = 0.027 μm–0.038 μm) and EDM treated surfaces (Ra = 1.08 μm–10.0 μm). The heat transfer coefficient of the roughest surface within the experiments was 210% higher than that of the polished surface. Yu et al. [9] fabricated micro cylindrical cavity arrays on a planar silicon plate using MEMS technology and found that the maximum CHF value of the 33 × 33 cavity array test surface was almost 2.5 times that of the planar silicon surface during the boiling test for FC-72. They also pointed out that for the heat transfer coefficient increased with the increase of heat flux and cavity density, but the higher the cavity density was, the smaller the critical heat flux was. In addition, in medium and high heat flux conditions, the surface with larger cavity diameter presented earlier attenuation and lower peak heat transfer coefficient. Može et al. [10] prepared the microstructure surface by hydrochloric acid chemical etching method, and hydrophobically treated the corroded aluminum surface with silane agent to form a functional hybrid aluminum surface with lower surface energy and improved surface microstructure. These surfaces enabled the early transition of bubbles to nucleation boiling. The heat transfer coefficient of the hydrophobically treated microcavity surface was 488% higher than that of the untreated reference surface. The pool boiling study carried out by Reed and Mudawar [11] showed the CHF increase of up to 400% on the copper based micro-fins surface and illustrated that the nucleate boiling heat transfer coefficient had nothing to do with the surface orientation relative to the gravity. Zhang and Ma [12] used dry etching technique to prepare single radial microcolumn surface and four radial microcolumn surfaces. Using FC-72 as working medium, experimental studies were carried out under four different degrees of liquid undercooling. The heat transfer characteristics for radial microcolumn surface was obviously improved, showing earlier nucleate boiling and higher heat transfer coefficient.

Some researchers also explored the continued fabrication of nanostructures on the basis of micro-processing to further improve the heat transfer performance of boiling surfaces. Jung et al. [13] fabricated silicon wafers as boiling surface with roughness from 163 nm to 307 nm by anodizing method and obtained the HTC values about 2200–4000W/m^2 K at CHF, which was much higher than that of ordinary surfaces. With the increase of surface area, more nucleation sites within that surface were provided, and the CHF was improved linearly. Wang et al. [14] used hydrogen bubble template deposition method and further applied low-density current method to fabricate two kinds of micro-and nano-porous surfaces, respectively. The heat transfer coefficient of the former was 2.8 times that of the flat surface, while that of the latter was 4.8 times that of the flat surface. The principle was that the lower interface of the phase modified surface can accelerate the separation of bubbles. Ray et al. [15] prepared TiO_2 nanowire with varied thickness on test surface by e-beam evaporator (EBE) and glancing angle deposition technique. Due to the increase of surface area as well as the roughness, especially thermocapillary effect due to the porous properties of surface modification, the wall superheat of R134a during initial boiling stage was reduced by 16.30%, 30.55% and 44.86% corresponding to the coating surface thickness of 150 nm, 300 nm and 450 nm, respectively. In order to further magnify the capillary effect, Cao et al. [16] prepared the modified porous composite surface by electrostatic deposition of FeMn oxidation nanoparticles. The wickability of FC-72 on the porous surface were analyzed by absorption flow method, which was considered to be the main mechanism for increasing the critical heat flux of pool boiling by more than 100%. Može et al. [17] prepared nanostructures on titanium foil by hydrothermal etching in alkaline solution, and the two surfaces were superhydrophobic by chemical vapor deposition of fluorinated silane. The heat transfer coefficients of hydrophobically treated spear and cavity surfaces were up to 89% and 237% higher than those of untreated reference surfaces, respectively. Besides, they used chemical oxidation treatment to functionalize the sample, and then hydrophobically treated the selected surface with fluorinated silane, which showed good manufacturing repeatability. Water, water/n-butanol mixture and Novec 649 were used as pool boiling working fluid. After treatment, the surface heat transfer coefficient and critical heat flux were enhanced by 120% and 64%, respectively [18]. Kumar et al. [19] used electrodeposition to attach a layer of copper nanowires on plain copper surface and effectively improved the heat transfer coefficient as well as the CHF value within the pool boiling experiments using FC-72. The reason for the enhancement was the increased density and size of the micron cavities during the growth of nanowires. Besides, they also found that super-hydrophilic properties, capillary effect and enhanced bubble dynamics parameters were also the coexistence mechanisms of performance improvement.

Though the above surface enhancement methods could effectively improve the pool boiling performance for dielectric fluids, there were still many limitations. For example, etching and electrochemical deposition methods often required large-scale processing equipment, which was not that suitable for the complex structure of the curved surface or inner wall for heat exchangers, and lacked reliability and durability. In addition, MEMS and NEMS technologies were still difficult to meet the requirements of large-scale applications for metal materials commonly used in heat transfer, and some of the processes were even only suitable for silicon-based materials. At the same time, the subtractive structure was almost non-replaceable, which undoubtedly increased the maintenance and upgrade cost, reducing the flexibility of the index including heat transfer performance.

For this reason, some scholars also tried to study the enhancement approach of pool boiling performance by directly coating porous structure/material above the heat transfer surface, which was simpler and more convenient for engineering application and popularization. Jo and Kim [20] sprayed reduced graphene oxide (RGO) sheets onto the copper surface at supersonic speeds. In the pool boiling experiments of FC-72, the CHF and HTC increased by 50% and 150%, respectively. It was believed that the high wettability of RGO film improved the cohesion between coolant and heated surface, and the rough surface of RGO film also provided more nucleation sites. Rainey et al. [21] coated diamond particles (8–12 μm) on copper substrate surface by epoxy bonding method. Their test results showed that the nucleate boiling performance of plain surface was related to the heater orientation, while the microporous coating surface was insensitive to the heater direction, which was also a significant advantage of the microporous surface. Sarangi et al. [22] tested the enhancement ability of sintered copper powder layer (45–1000 μm particle size) for heat transfer performance of FC-72 and found that while wall superheat decreased by 32%, the CHF increased by 44% compared with the free granular layer coating surface. They also pointed out that the optimum particle size of and the sintered coatings was about 100 μm. Manetti et al. [23,24] studied the properties of the modified heating surface composed of copper foam metal, and the pool boiling test was carried out under saturated conditions with HFE-7100 performing coolant function. Compared with the ordinary surface, the metal foam surface provided a higher heat transfer coefficient, and the highest heat transfer coefficient was 12,400 W/m^2 ·K at heat flux around 270 kW/m^2. At the same time, it prevented thermal

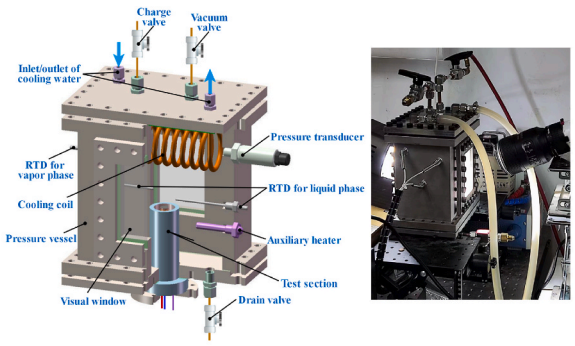

(a) Boiling device

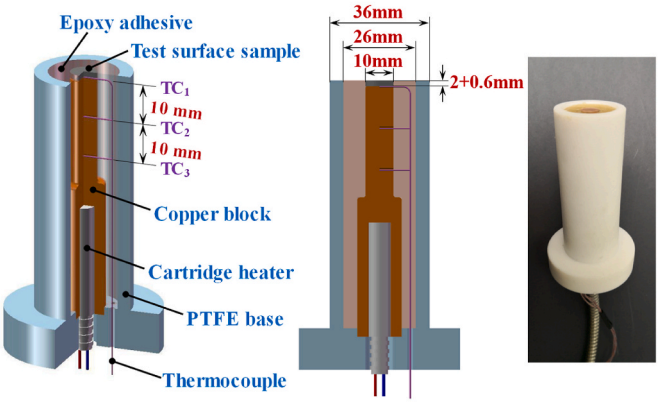

(b) Test section

Fig. 1. Experimental facility.

overshoot during initial nucleation boiling. They also pointed out that among the test surfaces, those with high thickness (2 mm and 3 mm) showed the best performance under the condition of lower heat flux and the one with the lowest thickness had the best performance at high heat flux, which could be explained according to the dominant heat transfer mechanism of copper foam surface that the heat transfer performance was affected by permeability, wettability, wickability and bubble dynamics together.

Therefore, the surface modification of direct coating method could also effectively improve the pool boiling heat transfer performance of dielectric fluids without the limitation of subtractive method. In particular, the method of sintering porous layer could adjust the porous structure characteristics of heat transfer surface coatings more flexibly, and has higher maneuverability and applicability in engineering application. However, how to effectively reduce contact thermal resistance for covered enhanced material and boiling surface and how to determine the optimal particle size still need to be further studied. In addition, as Cao et al. [16] pointed out, surface modification at the nano-level could further improve surface wettability and might increase the number of nucleation sites and capillary effect. If the micro-nano composite modification method was further adopted, such as nano-treatment of the sintered surface, it would also have the chance to obtain more excellent heat transfer characteristics. But now, the conclusions obtained from different scholars on the enhancement of boiling heat transfer at the micro and nano levels were not unified, and even have some differences [25]. Therefore, the influence mechanism of further nano-treatment also needed to be further explored.

In this paper, the pool boiling heat transfer characteristics of the surface covered by sintered copper powder with particle dimension of 30/65/110 μm was investigated. The effect by further nano-treatment on sintered porous layer was also explored. The working fluid for all the pool boiling tests was refrigerant R245fa, since it was regarded as the promising coolant for electronic equipment. The heat transfer characteristics was evaluated according to the boiling curve tendency as well as heat transfer coefficient variation of each tested surface sample. The bubble behavior were also captured and recorded as the visual results for the analysis of dominant heat transfer mechanism during every boiling stage. The pore size of the enhanced porous layer as well as the effect of nano-treatment were deeply compared and discussed in the present pool boiling study.

2. Experiments

2.1. Experimental facility

The experimental device capable of current research on pool boiling heat transfer performance for volatile fluids at above atmospheric pressure is schematically described in Fig. 1(a). The boiling test pressure vessel is mainly composed a rectangular stainless-steel cavity, the upper/bottom cover plates and the integrated test section. The integrated test section was assembled and sealed from the bottom cover plate to the vessel by fastening measures to facilitate replacement. A pair of visual windows arranged opposite to each other on the front and rear walls of the vessel allow illumination of light source and image acquisition of high-speed camera, respectively, to observe the boiling phenomena. The vacuum valve facilitates the vacuum treatment and the charge valve is used for the fluid filling of pressure vessel before the experiments. After each experiment, the test fluid was recovered through the drain valve. The cooling coil penetrated the upper cover plate and accessed the chiller, thus regulating the pressure within the vessel by condensing vapor phase during the boiling process. To monitor the temperature of vapor and liquid phase within the vessel, four resistance temperature detectors were inserted into the vessel at different horizontal heights and the measurement uncertainty was ±0.15 °C. The pressure transducer with the accuracy of ±0.25% was installed in the vapor phase region of the upper part of the vessel to measure the pressure during the boiling process. The auxiliary heater was arranged at the height that can be immersed in the liquid phase to assist in adjusting the saturation temperature of test fluid.

Fig. 1(b) displayed the detailed features of integrated test section for boiling experiments. A two-step cylindrical protruding copper rod was adopted as the heating block, and a cartridge heater was inserted in its lower part. Only the top surface ($D_s = 10$ mm) of copper rod was exposed and used as the heating surface for test boiling surfaces, since the copper rod was wrapped within the PTFE base with the thermal conductivity of 0.26 W/m K. The gap between side surface and base was filled and cured by epoxy adhesive ($k = 0.2$ W/m K). Therefore, the lateral heating effect was basically eliminated, which maximized the uniform transfer of heat flux along the axial direction of copper rod to its top surface. Three microholes with the diameter of 0.6 mm and depth of 5 mm were arranged at the top surface of copper rod and vertically below the top surface at every 10 mm to install the T type thermocouples (calibration accuracy ±0.10 °C), used to deduce the heat flux of the heating surface as well monitor the axial temperature. On the top surface, the micro hole with the inserted thermocouples was filled with the same substrate of copper material ($k = 398$ W/m K) by atomic diffusion welding and then milled flat to ensure the heating uniformity of the top surface as much as possible. The side microholes of the copper rod were perfused using silicone grease (OMEGA OT-201-2) with the thermal conductivity of 27.7 W/m K. All extension lines of thermocouple were drawn from the reserved micropore at the bottom of PTFE base.

2.2. Test boiling surface

Fig. 2(a) shows the test boiling surfaces with similar sandwich structure including plain copper sheet, silver welding pad and porous layer were used to explore the pool boiling enhancement mechanism of porous material using sintered copper powder particles. The welding

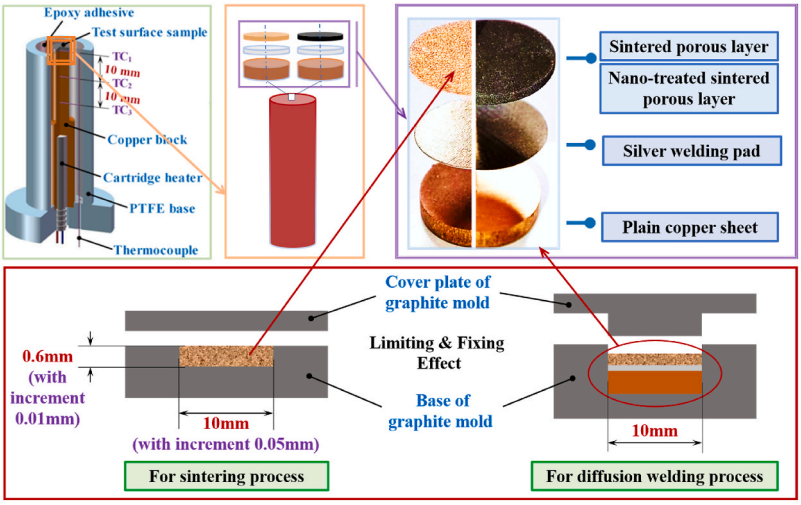

(a) The structure of test boiling surface and the graphite mold for sintering and diffusion welding process

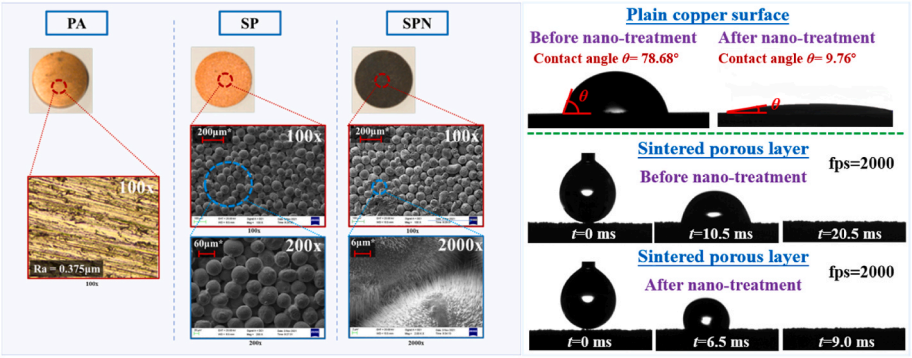

(b) Physical and SEM photos for test surfaces (PA/SP/SPN) and the wetting and wicking behavior on plain copper surface and sintered porous layer before and after nano-treatment

Fig. 2. The structure and characterization of test boiling surface.

pad (k = 410 W/m K) with the thickness of 0.1 mm was placed between the copper sheet and the copper powder porous layer, all of which were round samples with the same radius of 5 mm as the top surface of copper rod. The whole structure was placed in machined mold with graphite material for limiting as well as fixing, and then placed in the diffusion welding furnace for welding process with the protection of inert gas to prevent oxidation. The test boiling surfaces were all directly attached on the top surface of the copper rod using silicon grease with the thermal conductivity of 27.7 W/m K. Schematic diagram of graphite mold and its limiting and fixing effect was also given in Fig. 2(a). The whole structure for test surfaces was sandwiched between the base and the cover plate of the graphite mold, so as to ensure that there was no relative displacement between the plain copper sheet base, silver welding pad and the sintered porous layer and kept the three close to each other. The extra pressure did not need to be applied, so the welding process would not cause any obvious damage to the sintered porous layer. The existence of the welding pad significantly decreased the contact thermal resistance existed between copper sheet and sintered copper powder layers, and avoided the problems of low adhesion and easy shedding of the porous through the direct diffusion welding.

The spherical copper powder (30/65/110 μm) were selected to form the porous layers (SP-30, SP-65, SP-110) with the thickness of 0.6 mm by sintering process. It was well known that the porous layer of copper powder particles would have a certain geometric shrinkage compared with the original particle filling size after the sintering process, and the shrinkage was related to the particle size of copper powder. Therefore, based on the reference graphite mold of diameter 10 mm and depth 0.6 mm, a series of mold matrices with diameter increment 0.05 mm and depth increment 0.01 mm were customized to verify the shrinkage characteristics of porous layer caused by the sintering process shown in Fig. 2(a). Finally, the samples of sintered porous layer with the diameter of 10 mm and thickness of 0.6 mm were determined and selected for the pool boiling enhancement experiments. In the present study, the nano-treatment process was aimed at outer surface for spherical copper powder particles. For the integrity and non-destruction of nano-structure, the nano-treatment process was carried out after the completion of sintering process. Specifically, for the sintered porous layers of each size specification (SP-30, SP-65, SP-110), the compound porous layer (SPN-30, SPN-65, SPN-110) with burr-like nanostructure on copper powder particle surface was obtained by thermal oxidation treatment (480 °C, 150 min) in a muffle furnace. The copper powder particle surface with nanostructure formed by this treatment presented strong super hydrophilic characteristic as illustrated in this publication [26]. The physical pictures and SEM photos for the sintered copper powder layer samples before and after nano-treatment were partly given in Fig. 2(b). The porosity for each porous layer was obtained by weighing six identical samples and then calculating the ratio of the average value to the mass of the same volume solid sample. The suggested correlation of Kozeny–Carman equation [27] was used to calculate the permeability as recommended in several literatures [28,29]. As

Table 1
Characteristics of test boiling surfaces.

Surface type	Name	Roughness	Effective capillary radius	Permeability	Particle size	Porosity	Nanocrystalline treatment
			μm	K/m^2	μm	%	YES/NO
Plain surface	PA	Ra 0.375	/	/	/	/	NO
Copper powder covered surface	SP-30	On PA	8.3	8.3×10^{-13}	30	36.56	NO
	SPN-30	On PA	< SP-30	> SP-30	30	36.56	YES
	SP-65	On PA	34.5	8.9×10^{-12}	65	49.07	NO
	SPN-65	On PA	< SP-65	> SP-65	65	49.07	YES
	SP-65	On PA	106	2.3×10^{-11}	110	67.83	NO
	SPN-110	On PA	< SP-110	> SP-110	110	67.83	YES

for the effective capillary radius, it was calculated according to the ratio of the pore radius to the cosine of the contact angle [30]. Table 1 summarized the relevant parameters for all of the test boiling surfaces in the present study.

2.3. Experimental procedure

In the present pool boiling experiments, the refrigerant R245fa with the applicable temperature-pressure correspondence was adopted as the test fluid, which possessed the great potential as the coolant in the engineering application of electronic heat dissipation. Before each group of experiments, the pressure vessel was injected with the test liquid after vacuum treatment (vacuum pressure lower than 10 mbar), and the liquid level was kept at the position of 50 mm above the boiling surface. Then, the test fluid in the vessel would boil continuously at constant pressure for about 1.5 h to remove non-condensable gas from test fluid as well as the test boiling surfaces to improve the accuracy for boiling experiment. In the whole process of the experiments for each test surfaces, the saturation temperature for R245fa kept at around 20 ± 1.5 °C. Therefore, the corresponding saturation pressure was about 1.23 ± 0.07 bar. Through the matching control of the circulating cooling water in cooling coil in vapor phase region and the auxiliary heater in liquid phase region, the deserved inner pressure was slightly higher than that of saturation pressure corresponding to the saturation temperature, so as to ensure that the test liquid was in the subcooled state within the range of 2 °C. The boiling pressure of test fluid R245fa was measured in real time using pressure transducer during pool boiling process. This measure made the R245fa close enough to the saturated boiling state and avoided the interference of cavitation to the experimental results. For heating conditions, the interval of heating power grew with increasing heat flux and monitored by high precision power meter with the accuracy of 0.50%. At the beginning state, the interval was given in the range of 0.5–1 kW/m^2 for the capture the onset of nucleate boiling point. Then the interval continually raised with the value of 2 kW/m^2~5 kW/m^2 until the critical heat flux was reached. All data acquisition was conducted under the steady state for the boiling experiments.

Table 2
Uncertainties of test measurements and derived parameters including calculation methods.

Test measurements	Uncertainty	Derived parameters	Uncertainty
Dimensional accuracy	±5 μm	Effective heat flux	±0.78–7.10%
T type thermocouples	±0.10 °C	Surface temperature	±0.13–1.40%
Resistance temperature detectors	±0.15 °C	Heat transfer coefficient	±1.17–8.20%
Pressure transducer	±0.25%		
High precision power meter	±0.50%		

- $\frac{\delta q_{eff}}{q_{eff}} = \sqrt{\left(\frac{\delta T_1}{\Delta T_{13}}\right)^2 + \left(\frac{\delta T_3}{\Delta T_{13}}\right)^2 + \left(\frac{\delta L_{13}}{L_{13}}\right)^2}$
- $\frac{\delta T_s}{T_s} = \sqrt{\left(\frac{\delta T_1}{T_s}\right)^2 + \left(\frac{L_{s1}}{k_{Cu}} \bullet \frac{\delta q_{eff}}{T_s}\right)^2 + \left(\frac{q_{eff}}{k_{Cu}} \bullet \frac{\delta L_{s1}}{T_s}\right)^2 + \left(\frac{q_{eff} L_{s1}}{k_{Cu}^2} \bullet \frac{\delta k_{Cu}}{T_s}\right)^2}$
- $\frac{\delta h_b}{h_b} = \sqrt{\left(\frac{\delta q_{eff}}{\delta q_{eff}}\right)^2 + \left(\frac{\delta T_s}{T_s - T_{sat}}\right)^2 + \left(\frac{\delta T_{sat}}{T_s - T_{sat}}\right)^2}$

3. Data reduction

3.1. Heat transfer

Based on the Newton's cooling law, the heat transfer coefficient for the test boiling surfaces in the present pool boiling experiments was derived as follows:

$$h_b = \frac{q_{eff}}{T_s - T_{sat}} \tag{1}$$

where, T_{sat} denoted the saturation temperature of test fluid during the boiling process. The value was determined by the averaged measurements of the resistance temperature detectors in liquid phase zone avoiding the error of querying the saturated temperature based on corresponding pressure value.

And q_{eff} represented effective heat flux for the boiling surfaces, which was determined by 1D Fourier's law as follows:

$$q_{eff} = -k_{Cu}\frac{\Delta T_{13}}{L_{13}} \tag{2}$$

where, $\Delta T_{13} = T_3$-T_1 and L_{13} were the temperature difference and distance of $TC_3$and TC_1, respectively. The dimensional accuracy was ±5 μm in the present study. The R^2 values corresponding to the linear regression for the measurements of TC_1, TC_2 and TC_3 along the axis of copper rod were all greater than 99% at different heat flux during the boiling experiments in our previous study [31]. Thus, the radial heat loss for copper rod existed within the position of TC_1 and $TC_3$was approximately neglected. The derived effective heat flux based on TC_1 and TC_3 was reliable and avoided the relative error under low heat flux conditions when using TC_1 and TC_2. Besides, the maximum heat loss measured within the experimental conditions was only 4.53% with regard to the possible heat dissipation at the bottom of the test section, which could be estimated according to the ratio of effective heating powder to the actual input power of the cartridge heater within the experimental conditions of pool boiling tests in the present study.

T_s was the temperature of test boiling surfaces, which could also be estimated by Fourier's law according to the heating surface temperature from copper rod as follows:

$$T_s = T_1 - \frac{q_{eff} L_{s1}}{k_{Cu}} \tag{3}$$

where, T_1 represented the measured temperature by TC_1, i.e., the top surface of copper rod. L_{s1} denoted thickness of the copper sheet base attached on the heating surface, which was 2 mm for all test boiling surfaces, respectively. k_{cu} represented thermal conductivity for copper with the values of 398 W/m K. The thermal conductivity uncertainty for the copper sheet base was reasonably estimated to be 1% within the range of the test conditions in the present pool boiling experiments. It was worth noting that the temperature of test boiling surface referred to in the presented study was all on the basis of the top surface of 2 mm

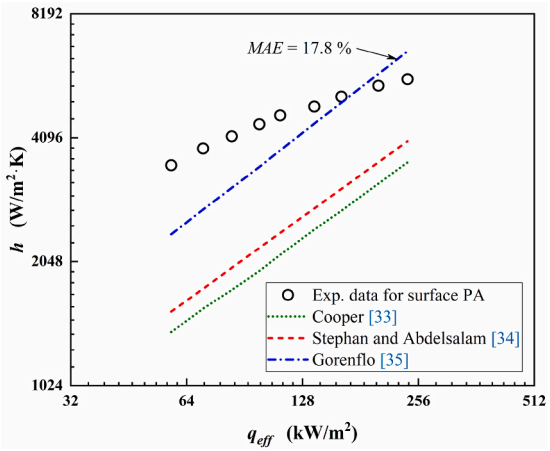

(a) Variation trend comparison between the experimental data and the widely used classical correlations for surface PA

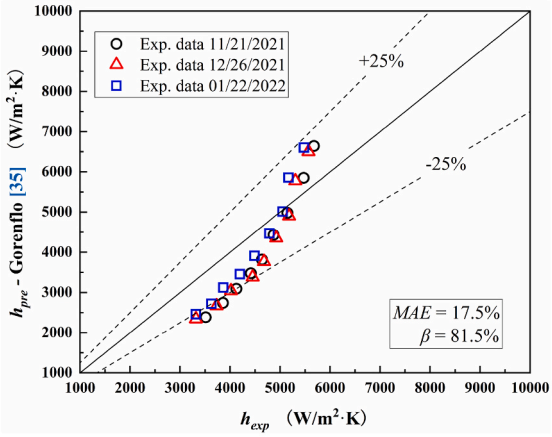

(b) Repeatability verification

Fig. 3. Validation of pool boiling experiments based on the plain copper surface.

thickness copper sheet base rather than that of porous layer. Because the porous layer was covered on top surface of the copper sheet base, the temperature at top surface of copper sheet base, i.e., the temperature for plain copper surface, was as reference for different test surfaces.

3.2. Uncertainty analysis

In this experiment, the calculation method proposed by Moffat [32] was used to analyze the uncertainty of the measured data. In this analysis, the effects of the accuracy of testing instruments such as copper column length and thermal conductivity, the temperature of thermocouple and RTDs and the range of experimental conditions on the uncertainty have been considered. The uncertainties of heat flux and surface temperature were calculated to be ±0.78–7.10% and ±0.13–1.40%, respectively. And that of pool boiling heat transfer coefficient resulted in ±1.17–8.20%. Table 2 listed the all uncertainties including test measurements and derived parameters in the present study. Besides, the calculation methods of the derived parameters were also attached in Table 2 as the reference. The above results showed that the experimental process has decent reliability and repeatability.

4. Results and analysis

4.1. Reliability verification of experiments

The confirmatory experiments on plain copper surface was carried out to verify the reliability of the present experimental device before the comparative study of the porous layer covered enhanced surfaces before and after nanostructure. Fig. 3(a) showed the variation trend of nucleate boiling heat transfer coefficient with effective heat flux on the plain copper surface and the corresponding comparison with the widely used classical correlations. In the logarithmic coordinate system, the variation trend of the heat transfer coefficient of plain copper surface with the effective heat flux was approximately linear, which illustrated that the experimental data were indeed in the satisfactory nucleate boiling stage and could be effectively used for the reliability verification. Considering the test fluid R245fa in this study, several more suitable nucleate boiling heat transfer correlations for refrigerants proposed by Cooper [33], Stephan and Abdelsalam [34] and Gorenflo [35]. were selected for comparative verification. Though the three correlations were in good agreement with the experimental data in terms of the overall tendency, the Gorenflo's correlation had the relatively better prediction accuracy with the mean absolute error (MAE) value of 17.8%. This was mainly because that the Gorenflo's correlation was proposed on the basis of Cooper's and Stephan and Abdelsalam's correlations, and took into account comprehensive factors such as roughness, and was further verified by a wider range of organic working fluids. In addition, in order to test the repeatability of the pool boiling experiments, the heat transfer coefficients of plain copper surface obtained from different experimental test time nodes were compared with the predicted values of Gorenflo's correlation as shown in Fig. 3(b). The results showed that 81.5% of the experimental data were within the deviation band of ±25% with the

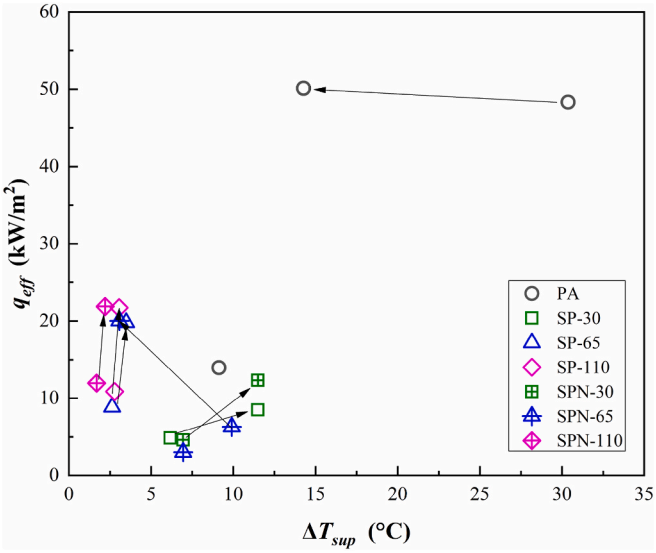

Fig. 4. ONB points of different boiling surfaces.

MAE value of 17.5%, which meant that the repeatability of the experiments was reasonable and acceptable. Thus, the above contents also proved the reliability of the experimental results in the present study.

4.2. Analysis of initial boiling state

With the increasing heat flux, the trigger phenomenon of onset of nucleate boiling (ONB) point for the surface PA was obviously captured during the experiments shown in Fig. 4. The test fluid of R245fa failed to boil before the heat flux reached 48.3 kW/m^2. At the same time, the corresponding wall superheat reached 30.4 °C. Afterwards, the boiling surface experienced a large temperature drop, reaching 14.3 °C.

However, for all of the porous layer covered surfaces tested, R245fa could be triggered to boil in a low heat flux range (4.59–11.9 kW/m^2) and the corresponding wall superheat were all less than 10 °C, since the existence of the micro/nano porous structures offered many effective nucleation sites for that boiling surface. The sintered porous surfaces of SP-65 and SP-110 showed the extremely close and low wall superheat (2.6 °C and 2.8 °C) at the ONB points while the ONB point trigger temperature for the surface with 30 μm particle size obviously lagged behind about 6.16 °C. As shown in the visual results of Fig. 5(a), the nucleation state for the surface SP-30 at ONB point was not as satisfactory as that of 65 μm and 110 μm. The too small pore size resulted from the inter-particle cavity of 30 μm not only brought relative larger bubble detachment resistance, but also affected the number of nucleation sites at the beginning state. In fact, the porosity and the effective capillary radius of sintered layer covered surface SP-30 were all smaller than that of SP-110 as listed in Table 1, and studies by many scholars have shown that effective scale for the nucleation sites was evaluated as 5 μm–200 μm. Therefore, whether from the point of view of porosity or effective capillary radius, the number and size range of the effective nucleation sites on the surface SP-30 had no obvious advantage in the initial stage of boiling.

After the process of nanostructure treatment, the SPN-30 and SPN-65 nano-surfaces presented the significant lag characteristic at the ONB points, and the initial nucleation state was also significantly suppressed as seen the bubble behavior in Fig. 5(b). This was mainly because the highly wetting characteristic of test fluid R245fa caused by its extremely low surface tension directly suppressed the occurrence of nucleation to a large extent. But after the ONB points, the wall superheat of the two surfaces (SPN-30, SPN-65) quickly fell back to the same level of the corresponding surfaces without the nano treatment (SP-30, SP-65), which meant that the negative effect of highly wetting characteristic almost disappeared. It's worth noting that the overall influence of the highly wetting characteristic of nanostructures on the surface SPN-110 with large effective nucleation sites was limited. On the contrary, the nanostructure might enrich the multi-level pore structure of porous layer and thus expanded the effective dimension range for the potential nucleation sites, and further advanced the ONB point at about 1.7 °C.

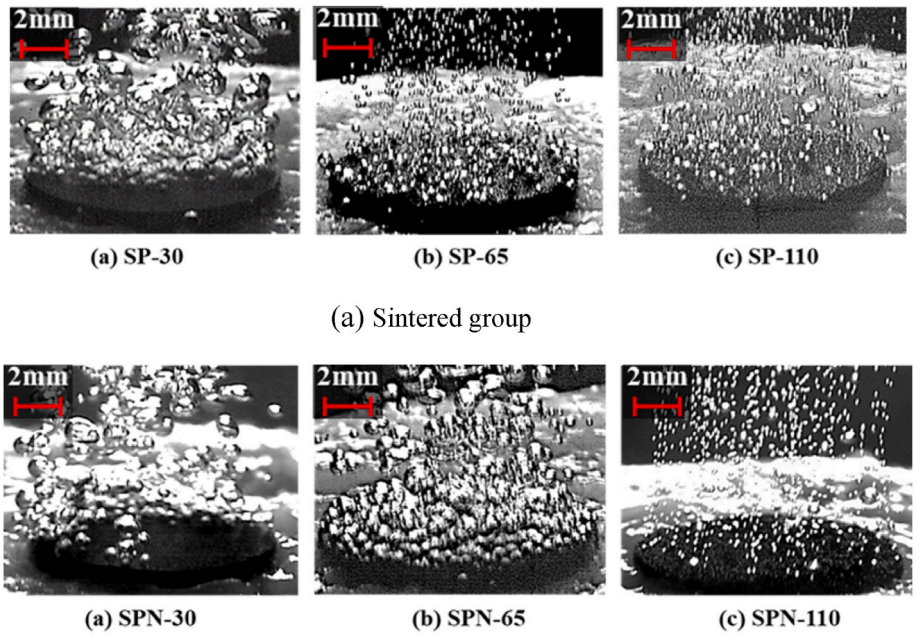

Fig. 5. Visual images at ONB points.

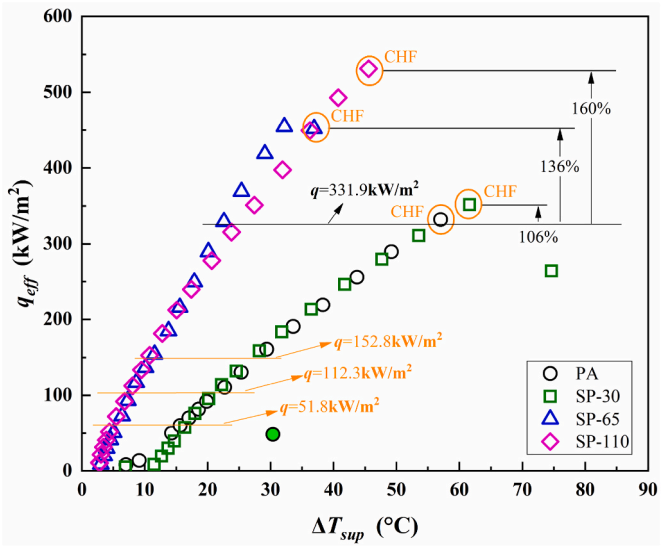

(a) Boiling curve (SP group)

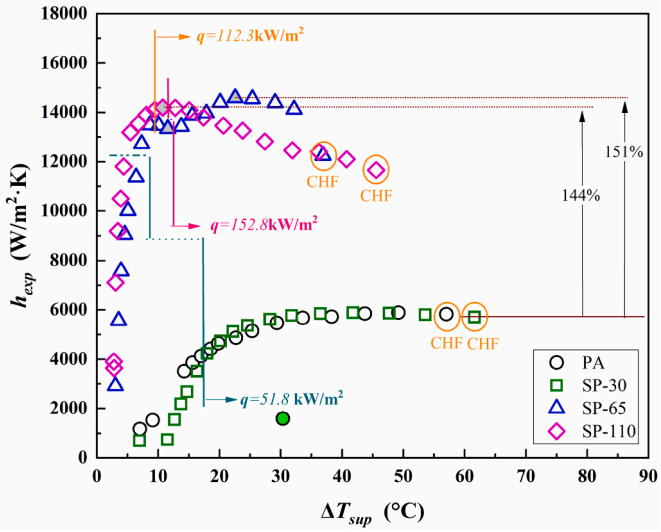

(b)Heat transfer coefficient (SP group)

Fig. 6. Boiling curves and HTC of sintered copper powder covered surfaces.

4.3. *Effect of particle size for sintered copper powder covered surfaces*

Fig. 6(a) and Fig. 6(b) presented the boiling curves and variation of heat transfer coefficient within the pool boiling experiments for the sintered porous surfaces (SP-30, SP-65 and SP-110) including the surface PA as the reference.

As shown in Fig. 6(b), the boiling heat transfer coefficient of enhanced surface SP-30 increased rapidly only at the initial boiling stage before $q_{eff} = 51.8$ kW/m^2. Fig. 7 shows the visualized bubble behavior for the boiling process of sintered layer covered surfaces. When the heat flux reached 154.2 kW/m^2, the HTC was basically stable at about 5847 kW/m^2 ·K until the occurrence of critical heat flux. The particle size of sintered copper powder on the surface of SP-30 was tiny, so the formed effective nucleation site number were too small, and the size range was very limited. Thus, the nucleation state would be easily saturated with the rising heat flux at initial stage. In addition, for the sintering process of copper powder with too small particle size, the phenomenon of particle adhesion was also easy to occur and always formed the blind pore area in the sintered porous layer, which not only affected the capillarity of the porous structure, but also increased its heat transfer resistance. Therefore, with the comparison of surface PA, the HTC of surface SP-30 had not been obviously enhanced, and the variation of the boiling curve was almost the same as that of the plain one, regardless of the contribution of porous effect to the ONB and CHF performance (up to 106% at CHF).

However, compared with the plain copper surface, the other two enhanced surfaces of SP-65 and SP-110 presented the excellent boiling heat transfer coefficient improvement with the maximum increase to 151% and 144%, respectively. These two sintered copper powder layers provided very abundant effective nucleation sites, which could be confirmed by the sharp exponential upward trend experienced by their curves of HTC with wall superheat before $q_{eff} = 51.8$ kW/m^2, respectively. Then, the rising tendency of the HTC of surface SP-65 and SP-110 would also slow down rapidly like the surface SP-30. It was mainly due to the fact that the dominant factor of heat transfer enhancement was transformed from the active number of nucleation sites to the bubble formation and separation rate after reaching the corresponding turning point heat flux. But the wall superheat at the turning point where the growth tendency of HTC for surface SP-65 and SP-110 slowed down were all close to 5.4 °C, which was much less than that of 17.0 °C for SP-30 at $q_{eff} = 51.8$ kW/m^2.

After the turning point heat flux, it could be seen some differences in the variation trend of heat transfer coefficient between surface SP-65 and SP-110. When the effective heat flux was greater than 112.3 kW/m^2, the heat transfer coefficient of surface SP-110 showed a continuous and slow declining trend, while the heat transfer coefficient of surface SP-65 went through the stagnation point ($q_{eff} = 152.8$ kW/m^2) after turning point heat flux of 112.3 kW/m^2. After the stagnation point, heat transfer coefficient of SP-65 increased obviously again. The most likely explanation for this phenomenon was that the increase of heat flux activated some potential nucleation sites such as small internal pores in porous layer or cavities on the surface of copper particles, forming the secondary nucleation characteristics. This also made the heat transfer performance of surface SP-65 was relatively higher than that of SP-110 at higher heat flux during this period.

However, within the experimental range of this study, due to the influence of flow resistance caused by relatively small pores in the porous layer, the surface SP-65 would still reach the critical heat flux earlier than SP-110, which depended on the boiling surface refreshing effect caused by the dynamic balance among liquid reflux resistance, bubble detachment resistance and capillary wicking effect.

Took the visualization results of the enhanced surface SP-30 and SPN-110 in Fig. 8 as an example, after the effective heat flux reached 351.7 kW/m^2 and 553.4 kW/m^2 respectively, the bubbles near the boiling surfaces gathered and merged violently, and the detachment deteriorated seriously, forming a huge vapor mass bubble region. The upward detachment process of the large bubbles under the action of buoyancy would cause the disturbance of the mainstream liquid. Under the effect of inertia, the liquid directly above the bubble further delayed its detachment. Therefore, the proportion of vapor phase stagnation time on the boiling surface increased, and the refresh rate of liquid in the porous layer decreased significantly, resulting in the obvious heat transfer crisis and almost approaching the arrival of critical heat flux. As shown in Fig. 6(a), compared with surface PA, the critical heat flux for the enhanced surface SP-65 and SP-110 increased by about 36% and 60%, respectively. The improvement for surface SP-30 was only 6%. The small number and very limited size range of effective nucleation sites for SP-30 led to the saturation of nucleation capacity at lower heat flux, which lowered the upper limit of CHF enhancement, though the existing nucleation sites could make the onset of boiling more easily than the plain one. As for surface SP-65 and SP-110, the increase of the number of nucleation sites in the effective size range and the decrease of the flow resistance in the porous layer were considered to be the key factors to the improvement the corresponding CHF values.

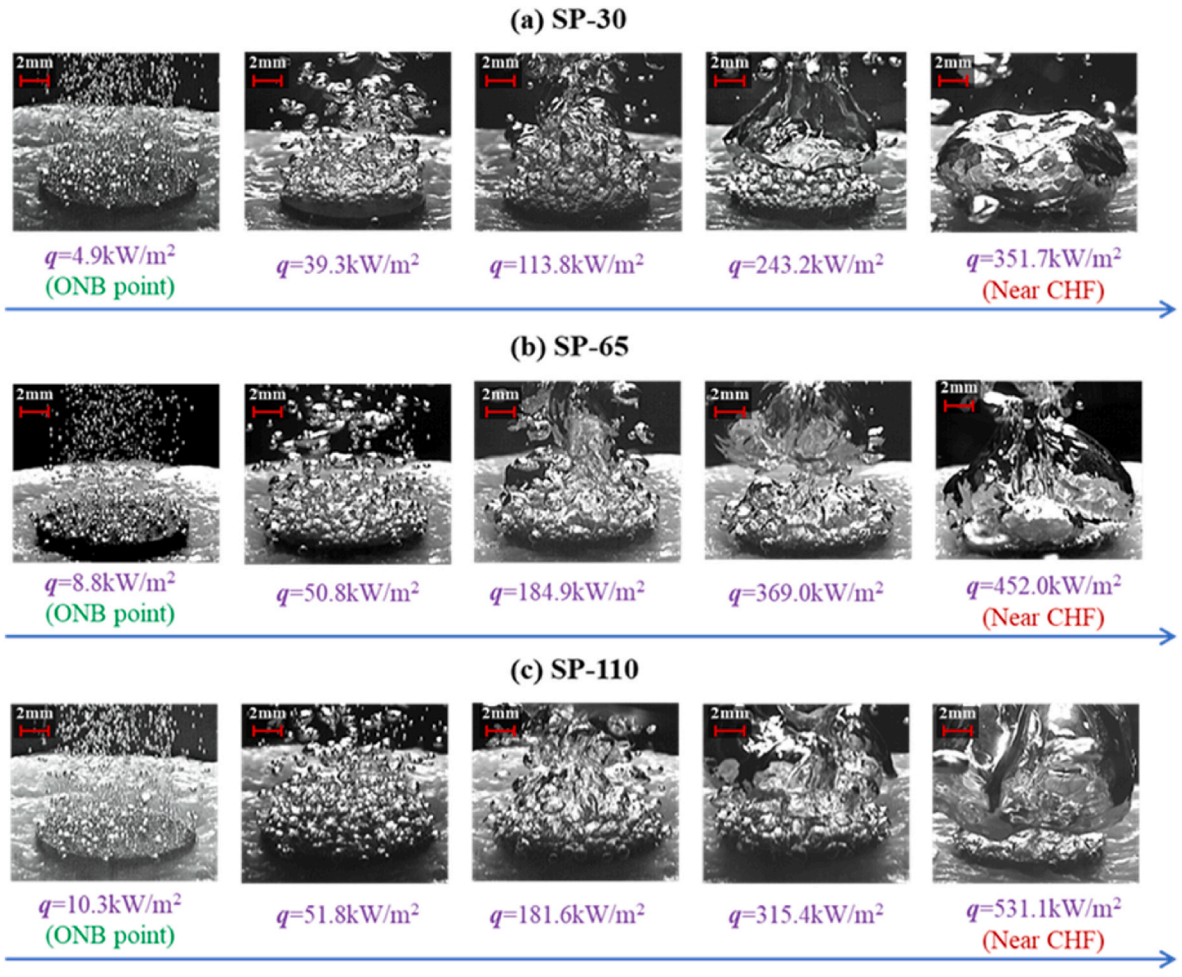

Fig. 7. Visualization results for pool boiling of sintered porous surfaces with different particle sizes.

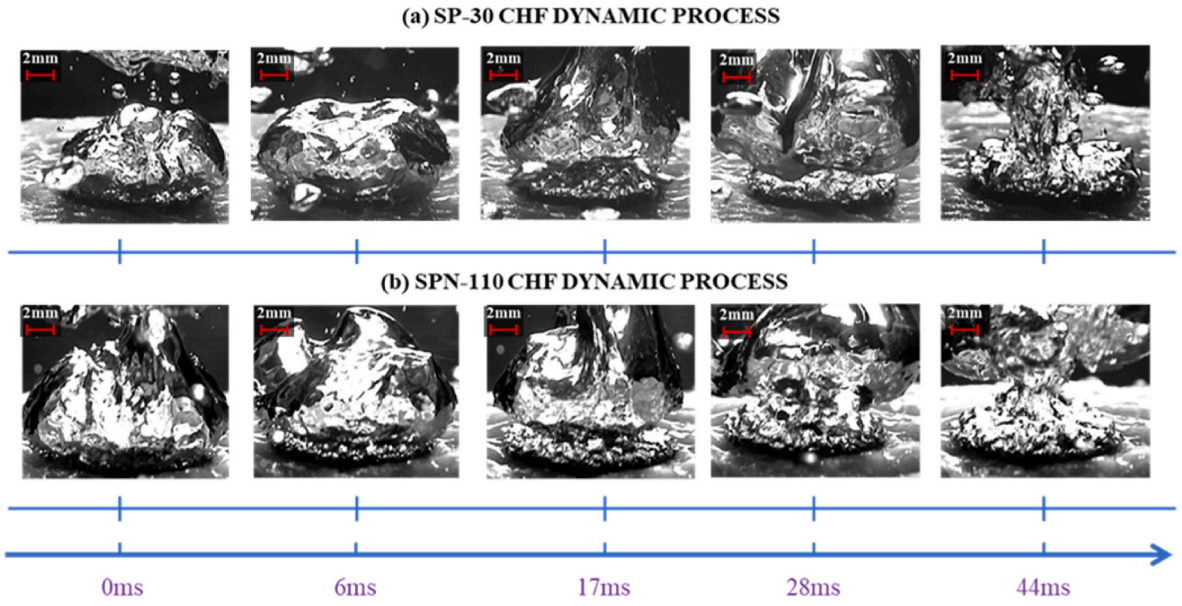

Fig. 8. Visualized CHF process on different surfaces.

4.4. *Effect of nano-treatment on sintered surface*

Fig. 9 depicted the boiling curve and the variation of heat transfer coefficient of the sintered porous surface composed of 30 μm copper powder particles with and without surface nano-treatment process. The heat flux and heat transfer coefficient for surface SPN-30 with nano

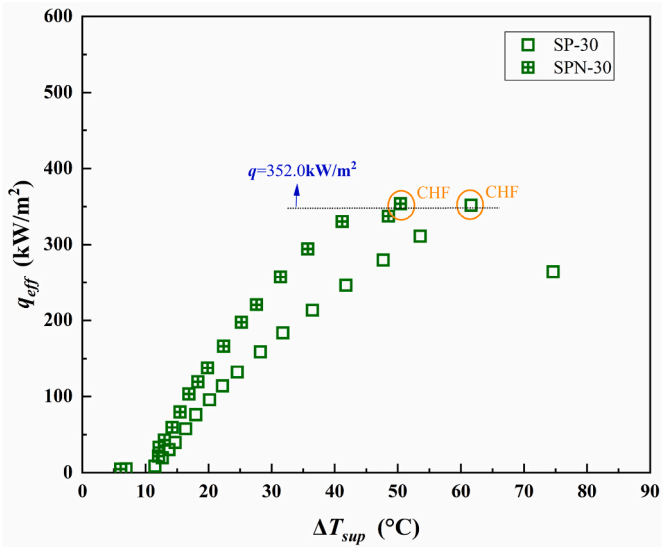

(a) Boiling curve (SPN-30)

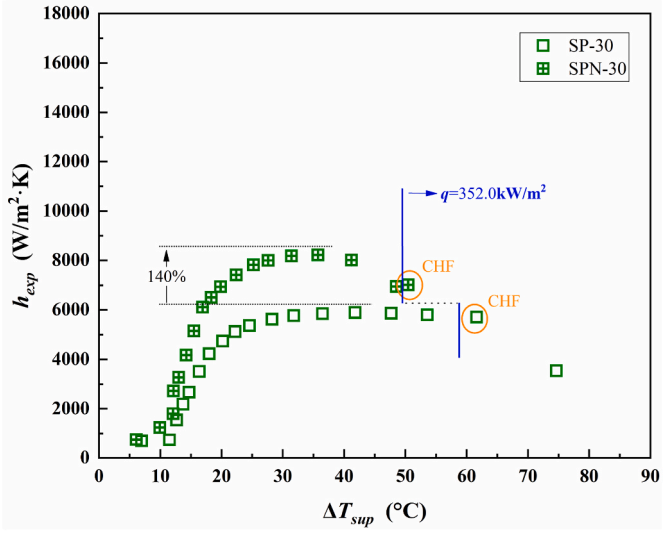

(b) Heat transfer coefficient (SPN-30)

Fig. 9. Boiling curves and HTC of nano-treated sintered porous surfaces SPN-30.

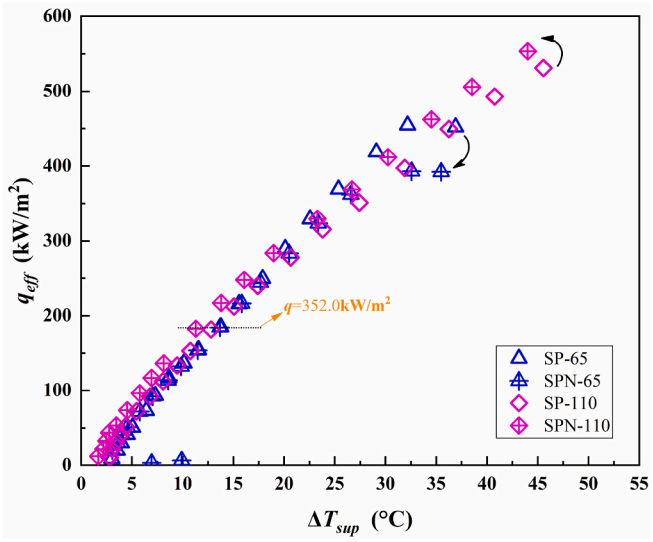

(a) Boiling curves (SPN-65, SPN-110)

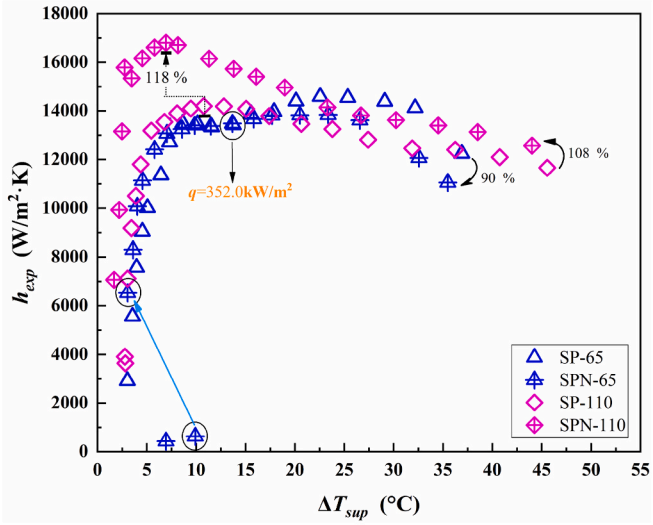

(b) Heat transfer coefficient (SPN-65, SPN-110)

Fig. 10. Boiling curves and HTC of nano-treated sintered porous surfaces SPN-65 and SPN-110.

structure were always slightly higher than those of surface SP-30 under the same wall superheat, and the maximum increase of HTC was about 140% at q_{eff} = 294.1 kW/m^2. But the boiling characteristics of the two surfaces maintained a similar trend, and finally reached the CHF points at a very close heat flux (q_{eff} = 352.0 kW/m^2). The surface nano-treatment process formed the dense burr-like nanostructures (Fig. 2 (b)) on the surface of copper powder particles, which in essence increased the surface area of the copper powder particles, and might lead to more potential nucleation sites. To some extent, this method made up for the negative effects of surface SP-30 without nano-treatment due to the small particle size of copper powder, such as particle adhesion formed by the sintering of porous layer as well as surface welding and regional blind hole caused by solder filling. Thus, surface SPN-30 had relatively better heat transfer performance at initial and stable stages during the boiling process. Nevertheless, the surface after nano-treatment in the Muffle furnace had the characteristics of super-hydrophilic, which would increase the detachment resistance of bubbles, and this effect would be more prominent in the case of violent bubble coalescence and worsening heat transfer deterioration at high heat flux conditions. Therefore, the heat transfer coefficient of SPN-30 decreased under high heat flux, and finally showed the similar CHF value to that of SP-30. This could also be proved from the content of Fig. 11, which showed the visualization results of pool boiling on nano-treated sintered copper powder surfaces to presented the bubble behavior. It was obvious that the bubble detachment diameter of surface SPN-30 was relatively larger even from the initial boiling stage with the comparison of surface SP-30 in Fig. 7, which implied the greater detachment resistance of bubbles for the surface SPN-30.

The heat transfer characteristics for enhanced surface SPN-65 and SPN-110 were shown in Fig. 10. With the comparison of sintered porous surface with 65 μm particle sizes, the nano-treated surface SPN-110 presented a better effect of boiling heat transfer enhancement. The pore size of sintered layer covered surface SPN-110 was already larger, and the composite nanostructure on the copper powder surface could not only increase the number of nucleation sites, but also further expanded the size range of the sites. Then, the HTC increased

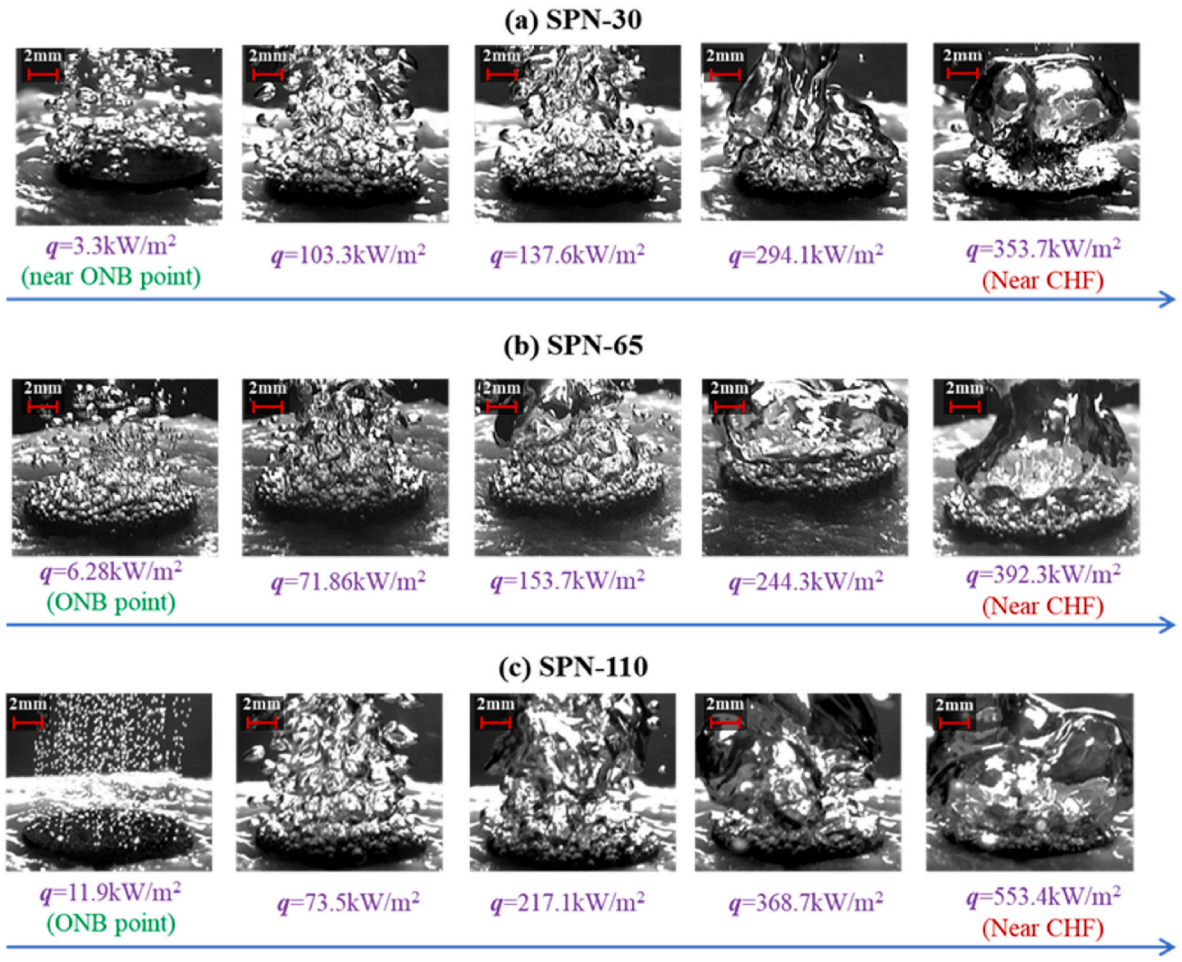

Fig. 11. Visualization results for pool boiling of nano-treated sintered porous surfaces.

significantly at initial boiling stage dominated by the heat transfer mechanism of rapid nucleation, with a maximum value of 118% at the turning point heat flux of 116.8 kW/m^2.

After turning point heat flux, the heat transfer enhancement caused by nano-treatment was still effective, but the degree began to decrease gradually. This was mainly due to the hydrophilic characteristics that help to further enhance the liquid replenishment ability of the porous layer under the condition of good bubble detachment during the stable boiling process, but at the same time, the corresponding effect of increasing bubble detachment resistance would also be gradually obvious under high heat flux. Referring to Fig. 11, from the point of view of bubble detachment resistance, we could also more intuitively find that after nano-treatment, the bubble detachment diameters of surfaces SPN-65 and SPN-110 were relatively larger compared with the corresponding visualization results in Fig. 7. In addition, the effect of bubble detachment diameters for the sintered porous surface with 65 μm particles was more obvious than 110 μm, either from the initial boiling stage or to the higher heat flux conditions. Nevertheless, due to the great inclusiveness of the larger pore size to the effective nucleation scale of the surface after the composite nanostructures, the corresponding CHF of the nano-treated surface SPN-110 was still improved by 8% compared to that of surface SP-110. The difference was that the heat transfer coefficient of the sintered porous surface with particle size of 65 μm was also enhanced at the initial stage of boiling after nano-treatment, but it was weakened after the turning point heat flux of 352.0 kW/m^2, and the CHF value was 10% smaller than that of the surface SP-65 without nano-treatment.

The most likely reason was that the highly wettability caused by the super-hydrophilic characteristics of nanostructures hindered the secondary nucleation of some potential small nucleation sites at high heat flux, which could be illustrated by the absence of the stationary point in Fig. 10(b). In essence, the pore size for sintered layer covered surface with 65 μm particle dimension was smaller than 110 μm, and the growth of nanostructure on the particle surface would further squeeze the pore space to some extent, which might reduce the number of nucleation sites with larger size that were easier to be activated.

5. Conclusion

The saturated pool boiling heat transfer characteristics for refrigerant R245fa were carried out on the sintered porous surfaces with and without nano-treatment. The effects of particle size and further nano-treatment of copper powder on the heat transfer enhancement were discussed. The following conclusions were obtained.

(1) The wall superheats at ONB point of all tested sintered porous surfaces were below 7 °C, which was much lower than that of 30 °C for plain copper surface. Particularly, the enhanced surface with sintered layer thickness 0.6 mm and particle size 110 μm was most likely to trigger nucleation process with the wall superheat as low as only 1.7 °C.
(2) The sintered porous surfaces of SP-65 and SP-110 had a wide size range of nucleation sites. Compared with surface PA, the maximum HTC raised to 151% and 144%, as well as the corresponding CHF value to 136% and 160% respectively. The continuous improvement of heat transfer performance of

enhanced surface SP-30 was limited due to the reduction of quantity as well as size range of nucleation sites.

(3) After nano-treatment, the heat transfer characteristics for all sintered porous surfaces increased again at medium and low effective heat flux accompanied by the smooth process of bubble nucleation and detachment. The maximum heat transfer coefficient raised to 140% of the non-nano-treated surface, while the CHF increased to 108% at most. However, relative heat transfer degradation occurred on the 65 μm surface with nano-treatment at the onset of boiling and high heat flux conditions. Not only the ONB point hysteresis was about 10 °C, but also the CHF value reduced by 10% compared with the non-treated one. The impact of nano-treatment on heat transfer enhancement for sintered porous surface was simultaneously affected by the particle size and the dominant heat transfer mechanism at different heat flux regions.

Author contributions

Chao Dang: Conceptualization, Investigation, Writing – original draft, Writing – review & editing. **Ruiqi Min**: Investigation, Validation, Data curation. **Lingyun Pan**: Investigation, Validation, Data curation. **Liaofei Yin**: Conceptualization, Investigation, Project planning. **Zhiqiang Zhang**: Validation, Data curation. **Yanxin Hu**: Validation, Data curation.

Declaration of competing interest

The authors declare that they have no known competing financial interests or personal relationships that could have appeared to influence the work reported in this paper.

Data availability

The authors do not have permission to share data.

Acknowledgments

This research was supported by the National Natural Science Foundation of China (No. U2141219, No. 52106069) and the Fundamental Research Funds for the Central Universities (No. 2022RC024).

References

[1] K.C. Leong, J.Y. Ho, K.K. Wong, A critical review of pool and flow boiling heat transfer of dielectric fluids on enhanced surfaces, Appl. Therm. Eng. 112 (2017) 999–1019.
[2] M. Issam, Recent advances in high-flux, two-phase thermal management, J. Therm. Sci. Eng. Appl. 5 (2013), 021012.
[3] A. Bar Cohen, P. McCluskey, P. Wang, Two-phase liquid cooling for thermal management of IGBT power electronic module, J. Electron. Packag. 135 (2013), 021001.
[4] M. Issam, Assessment of high-heat-flux thermal management schemes, IEEE Trans. Compon. Packag. Manuf. 24 (2001) 122–141.
[5] B. Tadej, V. Matevž, P. Tim, Z. Matevž, G. Iztok, Pool-boiling performance on thin metal foils with graphene-oxide-nanoflake deposit, Nanomaterials 12 (2022) 2772.
[6] J.Y. Ho, K.K. Wong, K.C. Leong, Saturated pool boiling of FC-72 from enhanced surfaces produced by Selective Laser Melting, Int. J. Heat Mass Tran. 99 (2016) 107–121.
[7] K. Ferjančič, M. Može, P. Križan, M. Bobič, I. Golobič, Subcooled critical heat flux on laser-textured stainless-steel ribbon heaters in pool boiling of FC-72, Int. J. Heat Mass Tran. 159 (2020), 120090.
[8] B.J. Jones, J.P. McHale, S.V. Garimella, The influence of surface roughness on nucleate pool boiling heat transfer, J. Heat Tran. 131 (2009), 121009.
[9] C.K. Yu, D.C. Lu, T.C. Cheng, Pool boiling heat transfer on artificial micro-cavity surfaces in dielectric fluid FC-72, J. Micromech. Microeng. 16 (2006) 2092–2099.
[10] M. Može, V. Vajc, M. Zupančič, R. Šulc, I. Golobič, Pool boiling performance of water and self-rewetting fluids on hybrid functionalized aluminum surfaces, Processes 9 (2021) 1058.
[11] S.J. Reed, M. Issam, Enhancement of boiling heat transfer using highly wetting liquids with pressed-on fins at low contact forces, Int. J. Heat Mass Tran. 40 (1997) 2379–2392.
[12] Y. Zhang, X. Ma, J. Zhou, Z. Lei, J. Wei, Experimental investigation of pool boiling heat transfer on the radial micro-pillar surfaces, Appl. Therm. Eng. 214 (2022), 118843.
[13] J.Y. Jung, H.Y. Kwak, Effect of surface condition on boiling heat transfer from silicon chip with submicron-scale roughness, Int. J. Heat Mass Tran. 49 (2006) 4543–4551.
[14] Y.Q. Wang, J.L. Luo, Y. Heng, D.C. Mo, S.S. Lyu, Wettability modification to further enhance the pool boiling performance of the micro nano bi-porous copper surface structure, Int. J. Heat Mass Tran. 119 (2018) 333–342.
[15] M. Ray, S. Deb, S. Bhaumik, Pool boiling heat transfer of refrigerant R-134a on TiO2 nano wire arrays surface, Appl. Therm. Eng. 107 (2016) 1294–1303.
[16] Z. Cao, B. Liu, C. Preger, et al., Pool boiling heat transfer of FC-72 on pin-fin silicon surfaces with nanoparticle deposition, Int. J. Heat Mass Tran. 126 (2018) 1019–1033.
[17] M. Može, A. Hadžić, M. Zupančič, I. Golobič, Boiling heat transfer enhancement on titanium through nucleation-promoting morphology and tailored wettability, Int. J. Heat Mass Tran. 195 (2022), 123161.
[18] M. Može, V. Vajc, M. Zupančič, I. Golobič, Hydrophilic and hydrophobic nanostructured copper surfaces for efficient pool boiling heat transfer with water, water/butanol mixtures and novec 649, Nanomaterials 11 (2021) 3216.
[19] G. Udaya Kumar, S. Suresh, M.R. Thansekhar, et al., Effect of diameter of metal nanowires on pool boiling heat transfer with FC-72, Appl. Surf. Sci. 423 (2017) 509–520.
[20] H.S. Jo, M.-W. Kim, T.G. Kim, et al., Supersonically spray-coated copper meshes as textured surfaces for pool boiling, Int. J. Therm. Sci. 132 (2018) 26–33.
[21] K.N. Rainey, S.M. You, Effects of heater size and orientation on pool boiling heat transfer from microporous coated surfaces, Int. J. Heat Mass Tran. 44 (2001) 2589–2599.
[22] S. Sarangi, J.A. Weibel, S.V. Garimella, Effect of particle size on surface-coating enhancement of pool boiling heat transfer, Int. J. Heat Mass Tran. 81 (2015) 103–113.
[23] L.L. Manetti, A.S.O.H. Moita, R.R. de Souza, et al., Effect of copper foam thickness on pool boiling heat transfer of HFE-7100, Int. J. Heat Mass Tran. 152 (2020), 119547.
[24] L.L. Manetti, G. Ribatski, R.R. de Souza, et al., Pool boiling heat transfer of HFE-7100 on metal foams, Exp. Therm. Fluid Sci. 113 (2020), 110025.
[25] U. Sajjad, A. Sadeghianjahromi, H. MuhammadAli, C.-C. Wang, et al., Enhanced pool boiling of dielectric and highly wetting liquids – a review on surface engineering, Appl. Therm. Eng. 195 (2021), 117074.
[26] Z. Cui, L. Jia, Z. Wang, et al., Thermal performance of an ultra-thin flat heat pipe with striped super-hydrophilic wick structure, Appl. Therm. Eng. 208 (2022), 118249.
[27] J. Bear, Dynamics of Fluids in Porous Media, Dover Publications, New York, 1988.
[28] F.A. Dominguez Espinosa, T.B. Peters, J.G. Brisson, Effect of fabrication parameters on the thermophysical properties of sintered wicks for heat pipe applications, Int. J. Heat Mass Tran. 55 (2012) 7471–7486.
[29] S. Sarangi, J.A. Weibel, S.V. Garimella, Quantitative evaluation of the dependence of pool boiling heat transfer enhancement on sintered particle coating characteristics, J. Heat Tran. 139 (2017), 021502.
[30] D. Huang, L. Jia, Study on capillary properties of liquid absorption core of sintered copper powder, J. Eng. Thermophys. 42 (2021) 494–503.
[31] C. Dang, Y. Ding, Z. Qi, et al., Experimental investigation of saturated nucleate pool boiling heat transfer characteristics of R245fa on a copper foam covered surface, Int. J. Heat Mass Tran. 179 (2021), 121740.
[32] R.J. Moffat, Describing the uncertainties in experimental results, Exp. Therm. Fluid Sci. 1 (1988) 3–17.
[33] M.G. Cooper, Heat Flow Rates in Saturated Nucleate Pool Boiling-A Wide-Ranging Examination Using Reduced Properties, Advances in Heat Transfer vol. 16, Academic Press, 1984, pp. 157–239.
[34] K. Stephan, M. Abdelsalam, Heat transfer correlations for natural convection boiling, Int. J. Heat Mass Tran. 23 (1980) 73–87.
[35] D. Gorenflo, State of the art in pool boiling heat transfer of new refrigerants, Int. J. Refrig. 24 (2001) 6–14.